Concentric Eyewall Asymmetries in Hurricane Gonzalo (2014) Observed by Airborne Radar

ANTHONY C. DIDLAKE JR.

Department of Meteorology and Atmospheric Science, The Pennsylvania State University, University Park, Pennsylvania

GERALD M. HEYMSFIELD

NASA Goddard Space Flight Center, Greenbelt, Maryland

PAUL D. REASOR

Hurricane Research Division, NOAA/Atlantic Oceanographic and Meteorological Laboratory, Miami, Florida

STEPHEN R. GUIMOND

NASA Goddard Space Flight Center, Greenbelt, and Earth System Science Interdisciplinary Center, University of Maryland at College Park, College Park, Maryland

ABSTRACT

Two eyewall replacement cycles were observed in Hurricane Gonzalo by the NOAA P3 Tail (TA) radar and the recently developed NASA High-Altitude Imaging Wind and Rain Airborne Profiler (HIWRAP) radar. These observations captured detailed precipitation and kinematic features of Gonzalo's concentric eyewalls both before and after the outer eyewall's winds became the vortex maximum winds. The data were analyzed relative to the deep-layer environmental wind shear vector. During the beginning eyewall replacement cycle stages, the inner and outer eyewalls exhibited different asymmetries. The inner eyewall asymmetry exhibited significant low-level inflow, updrafts, and positive tangential acceleration in the downshear quadrants, consistent with observational and theoretical studies. The outer eyewall asymmetry exhibited these features in the left-of-shear quadrants, further downwind from those of the inner eyewall. It is suggested that the low-level inflow occurring at the outer but not at the inner eyewall in the downwind regions signals a barrier effect that contributes to the eventual decay of the inner eyewall. Toward the later eyewall replacement stages, the outer eyewall asymmetry shifts upwind, becoming more aligned with the asymmetry of the earlier inner eyewall. This upwind shift is consistent with the structural evolution of eyewall replacement as the outer eyewall transitions into the primary eyewall of the storm.

1. Introduction

Eyewall replacement cycles in hurricanes are notable events in which the storm's inner core undergoes major structural changes. In an eyewall replacement cycle, a newer, contracting outer eyewall replaces an older, decaying inner eyewall. Accompanying these structural changes are characteristic changes in the storm's maximum intensity, which have been well studied in previous work (e.g., Willoughby et al. 1982; Black and Willoughby 1992; Houze et al. 2006, 2007; Sitkowski et al. 2011; Yang et al. 2013). Given the elaborate processes of eyewall replacement, many studies focus on individual stages of the cycle—from formation of the outer, or secondary, eyewall (e.g., Qiu and Tan 2013; Sun et al. 2013) to decay of the inner eyewall (Sitkowski et al. 2012). Dynamical analyses of each stage are often conducted in an axisymmetric framework, as this framework captures important governing processes. Still, past studies suggest that throughout eyewall replacement, asymmetries also play a significant role that needs to be fully examined.

Corresponding author e-mail: Anthony C. Didlake Jr., didlake@psu.edu

Secondary eyewall formation begins an eyewall replacement cycle when inward-spiraling rainbands coalesce outside of the preexisting primary eyewall, forming a ring of convection that also contains an axisymmetric maximum in tangential wind (Dodge et al. 1999; Didlake and Houze 2011; Bell et al. 2012). Several hypotheses have been proposed for explaining the dynamics of this process, yet no consolidated theory currently exists. Examples involve vortex Rossby wave–mean flow interaction (Montgomery and Kallenbach 1997), boundary layer spinup due to unbalanced dynamics (Huang et al. 2012; Abarca and Montgomery 2013, 2014; Qiu and Tan 2013; Sun et al. 2013), and boundary layer spinup due to a feedback between linearized frictional convergence, convection, and radial vorticity (Kepert 2013). Many hypotheses invoke axisymmetric processes that occur outside of the primary eyewall when enough convective-scale and mesoscale rainbands and their associated dynamics project strongly onto the azimuthal mean (Judt and Chen 2010; Rozoff et al. 2012; Zhu and Zhu 2014). Didlake and Houze (2013a) and Qiu and Tan (2013) directly connect the dynamics of rainband asymmetries to important axisymmetric processes. To fully grasp the critical dynamics, a deeper understanding of asymmetries is needed during these early stages of an eyewall replacement cycle.

Once a secondary eyewall clearly manifests itself, its further strengthening and contraction can be explained by axisymmetric dynamics through both unbalanced boundary layer dynamics and balanced response arguments. Shapiro and Willoughby (1982) showed that an axisymmetric heat source representative of eyewall convection induces a balanced response that leads to contraction of the radius of maximum wind. While this result models the contraction of a single eyewall, the contraction and strengthening of a secondary eyewall would be governed by the same dynamics. Still, unbalanced dynamics in the boundary layer may play a crucial role; Abarca and Montgomery (2015) argued that boundary layer supergradient flow in a mature secondary eyewall plays a larger role than the balanced response in the contraction of the secondary eyewall. While these studies examined the evolution of an eyewall due to axisymmetric dynamics, it is well known that the eyewall typically has an asymmetric distribution of convection. Modeling, observational, and theoretical studies all indicate that the primary cause of eyewall asymmetries is a response to the environmental wind shear and resulting vertical tilt of the vortex (e.g., Jones 1995; Frank and Ritchie 1999; Reasor and Eastin 2012). When concentric eyewalls occur in a storm, observations also indicate an asymmetric distribution of convection within the secondary eyewall (Hence and Houze 2011).

However, the contribution of these asymmetries in the secondary eyewall evolution has yet to be thoroughly examined.

Previous studies have shown that the contracting, strengthening secondary eyewall supplants the older, primary eyewall. The exact processes responsible for the decay of the inner eyewall have been attributed to several mechanisms. Based on the balanced response arguments of Shapiro and Willoughby (1982), Willoughby et al. (1982) and Willoughby (1988) suggested that forced upper-level inflow and descent emanating from secondary eyewall convection occurs radially inward and counteracts the outflow of the inner eyewall. Rozoff et al. (2008) hypothesized that the increasing inertial stability of the secondary eyewall impinges upon upper-level outflow of the inner eyewall. Other studies hypothesize that forced convergence in the boundary layer gradually prevents the inflow from advancing inward past the secondary eyewall, thereby cutting off the high-θ_e air from the inner eyewall (Samsury and Zipser 1995; Zhu et al. 2004; Bell et al. 2012; Zhu and Zhu 2014). Each of these processes can disrupt the inner eyewall's overturning circulation, and thus lead to its collapse. Yet the relative role of each process remains unclear.

Detailed observations of an eyewall replacement cycle at all stages are crucial for advancing knowledge of their underlying dynamics. Yet, such observations are limited by the planning and resources needed to deploy instruments and platforms capable of useful data collection. In October 2014, observations were collected of Hurricane Gonzalo in a joint effort from three federal laboratories: NOAA's Hurricane Research Division, NASA's Goddard Space Flight Center, and the Naval Research Laboratory. On two consecutive days, airborne radars observed two eyewall replacement cycles, detailing the inner-core reflectivity and kinematic structures at different stages of eyewall replacement. This study will examine these observations to analyze the dynamics and evolution of the asymmetric features in concentric eyewalls. The data were collected by NOAA's P3 Tail (TA) radar and by NASA's High-Altitude Imaging Wind and Rain Airborne Profiler (HIWRAP) radar. The P3 TA radar has collected data for over three decades, proving instrumental to advancing tropical cyclone science (Aberson et al. 2006). HIWRAP is a recently developed Doppler radar system designed to obtain three-dimensional wind and precipitation fields from high-altitude aircraft (Li et al. 2016). Collected by aircraft that flew missions staggered in time, these observations will shed light on the concentric eyewall dynamics at different stages of the replacement cycle. In the following sections, we will consistently refer to the developed secondary eyewall as the outer eyewall even toward the

later stages of an eyewall replacement cycle when this eyewall becomes the primary eyewall of the storm. Also, the older, original eyewall will be called the inner eyewall throughout. Sections 2 and 3 describe the radar observations and analysis methods in the context of Hurricane Gonzalo's life cycle. Sections 4 through 7 examine the data from the four aircraft missions over two days. Section 8 discusses the results in the context of previous studies and section 9 presents the conclusions from the current study.

2. Data and methodology

The airborne radar data analyzed in this study were obtained during three different field campaigns in 2014. As part of NOAA's Intensity Forecasting Experiment (IFEX), the NOAA P3 N43 aircraft was deployed into Gonzalo each day on 15–17 October. This plane was equipped with the X-band TA Doppler radar. The TA radar scans around a horizontal axis and utilizes the fore/aft scanning technique (FAST; Jorgensen and DuGranrut 1991), collecting two independent looks at the three-dimensional wind vector as the plane flies along its track.

The P3 TA radar data were processed using an automated algorithm (Gamache 1997) that produces three-dimensional reflectivity and wind fields. The data first undergo an automated quality control and de-aliasing processes that produce errors comparable with those from manual quality control and de-aliasing (Rogers et al. 2012). Next, the wind fields are obtained using a variational technique (Gao et al. 1999; Reasor et al. 2009) that optimizes the radar projection equation while constrained by mass continuity and boundary conditions. These fields were solved onto a Cartesian grid with grid spacing of 2 km in the horizontal and 0.5 km in the vertical. Several past studies have utilized this automated algorithm for P3 TA radar analyses (e.g., Stern and Nolan 2009; Rogers et al. 2012, 2015; Reasor et al. 2013).

The HIWRAP radar was deployed as part of NASA's multiyear Hurricane and Severe Storm Sentinel (HS3) field campaign (Braun et al. 2016). In 2014, HS3 teamed with the Office of Naval Research's Tropical Cyclone Intensity (TCI) experiment to install HIWRAP onto NASA's WB-57 aircraft. The WB-57 flew into Hurricane Gonzalo daily during 15–17 October with an average altitude over the storm of 18.5 km. HIWRAP is a dual-beam, Ka- and Ku-band Doppler radar. Unlike the TA radar, HIWRAP's beams point downward at two different tilt angles and scan conically around a vertical axis. During the conical scan, the beams obtain multiple looks at the wind field, allowing for retrieval of the full three-dimensional winds. More HIWRAP details can be found in Li et al. (2016). HIWRAP was designed to fly on board the Global Hawk unmanned aerial vehicle, which is a high-endurance, high-altitude aircraft capable of flight times greater than 24 h. HIWRAP flew for the first time in 2010 on the Global Hawk during the Genesis and Rapid Intensification Processes (GRIP) field experiment (Braun et al. 2013; Guimond et al. 2016). While the endurance of the WB-57 is lower, it is a capable high-altitude platform for HIWRAP to collect valuable kinematic information of tropical cyclones throughout the depth of the troposphere.

Since its first deployment in 2010, the HIWRAP radar has undergone significant advances that included improved signal processing and reduced side-lobe interference. The processing of HIWRAP data begins with calibration, de-aliasing, and quality control editing. The three-dimensional wind fields are retrieved using the technique developed by Guimond et al. (2014). This technique is a variational scheme similar to that used for the TA radar except that it is modified to fit the HIWRAP scanning geometry. Results from this retrieval were compared with other recently developed wind retrieval algorithms for HIWRAP (Didlake et al. 2015; Tian et al. 2015), which all yielded similar qualitative results. The wind fields were solved onto a Cartesian grid with horizontal grid spacing of 2 km and vertical spacing of 0.5 km.

After the winds were retrieved on a Cartesian grid, they were interpolated to storm-centered cylindrical coordinates with a radial, vertical, and azimuthal resolution of 2 km, 1 km, and 0.5°, respectively. The storm motion was then removed from the winds. For the P3 data, storm centers were objectively determined using a real-time analysis of flight level data (Willoughby and Chelmow 1982). For the HIWRAP data, storm centers were subjectively determined using a combination of GOES satellite data and the HIWRAP reflectivity and wind data. These subjectively determined centers were much better than the standard storm center databases, and the qualitative results from this study were not sensitive to small deviations in the determined centers.

Additional data used in this analysis come from flight level observations collected by U.S. Air Force (USAF) C-130 reconnaissance aircraft, which flew in between the flight times of the WB-57 and P3. Vigh et al. (2016) recently developed the FLIGHT+ dataset, which gathers all NOAA and USAF flight-level data dating back to 1997. In this dataset, flight tracks are segmented into radial legs relative to the storm center determined by the method of Willoughby and Chelmow (1982). The flight-level data examined in this study were collected at the 700-hPa level, which ranges between 2.5- and 3-km altitude. We analyze all data with respect to the
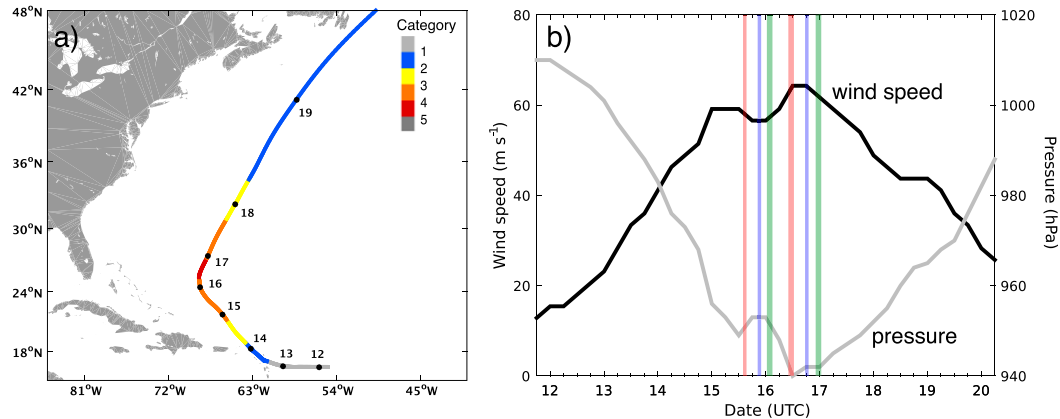
FIG. 1. (a) Best track of Hurricane Gonzalo from the National Hurricane Center with dates (UTC) in October 2014 marked. The Saffir–Simpson hurricane wind scale category is also indicated in color. (b) Central pressure and maximum wind speed throughout the lifetime of Gonzalo. Vertical lines mark the investigation times for the various aircraft. Red is for the NOAA P3 (TA radar), blue is for the NASA WB-57 (HIWRAP radar), and green is for the USAF C-130.

850–200-hPa deep-layer environmental vertical wind shear, which is taken from the Statistical Hurricane Intensity Prediction Scheme (SHIPS) database (DeMaria et al. 2005).

3. Storm and aircraft mission overview

Figure 1 shows the storm track, maximum wind speed, and central pressure for the life span of Hurricane Gonzalo. Gonzalo began as a typical Cape Verde tropical wave. As it approached the Lesser Antilles on 12 October, it strengthened from a tropical depression to a hurricane in 36 h and caused serious damage in the northeastern Lesser Antilles. Gonzalo continued to strengthen through 15 October when it reached 115-kt ($59.2 \, \text{m s}^{-1}$) winds and subsequently weakened slightly. During this time, Gonzalo began to interact with an approaching trough that turned the storm motion from northwest to north-northeast. Subsequently, Gonzalo restrengthened to reach its maximum intensity, 125 kt ($64.3 \, \text{m s}^{-1}$) with a central pressure of 940 hPa (category 4). Increasing shear caused Gonzalo to weaken steadily, but not before it crossed directly over Bermuda as a category 2 hurricane.

The oscillations in intensity occurring on 15 October and 16 October were associated with two distinct eyewall replacement cycles. Figure 2 displays microwave satellite images at select times on these two days, showing the distribution of heavy precipitation beneath the cirrus canopy. The NOAA P3, NASA WB-57, and USAF C-130 flew missions into Gonzalo on both 15 October and 16 October at the times listed in Table 1 and indicated in Fig. 1. Figure 3 displays the axisymmetric tangential winds from both the radar and flight-level datasets. At

0926 UTC 15 October, Gonzalo had a small, intense eyewall surrounding a 10-km-diameter eye. Outside the eyewall, a large rainband extended from the southeast and spiraled inward into a nearly circular band, indicating the development of a secondary, outer eyewall. At 1235 UTC, the inner eyewall remained at a small radius and the outer eyewall exhibited heavier precipitation mixed with the inner eyewall precipitation (Fig. 2). A local minimum of central pressure occurred at 1200 UTC (Fig. 1). At 1445 UTC, a secondary maximum in tangential winds appears near 45-km radius. By 1805 UTC, this secondary tangential wind maximum is now the only wind maximum and has contracted to a smaller radius, indicating the completion of an eyewall replacement cycle.

The eyewall replacement cycle on the next day had a more evident signal in the satellite imagery (Fig. 2). At 1129 UTC, a nearly circular band of precipitation clearly indicated the development of an outer eyewall. Flight-level data indicated that this developing outer eyewall did not yet exhibit a secondary tangential wind maximum. At 1200 UTC, Gonzalo reached its lifetime maximum intensity and lowest central pressure (Fig. 1). The outer eyewall strengthened by 1617 UTC and the older, inner eyewall became open to the southwest indicating its ongoing decline. By 2037 UTC, the outer eyewall tangential wind maximum had become the overall wind maximum, and by 2334 UTC, the inner eyewall had completely decayed and the eyewall replacement cycle was complete. The first replacement cycle occurred prior to Gonzalo's change in track to the northeast, and the second replacement cycle occurred as the storm was recurving. This timing suggests that the track recurvature did not influence either replacement cycle.
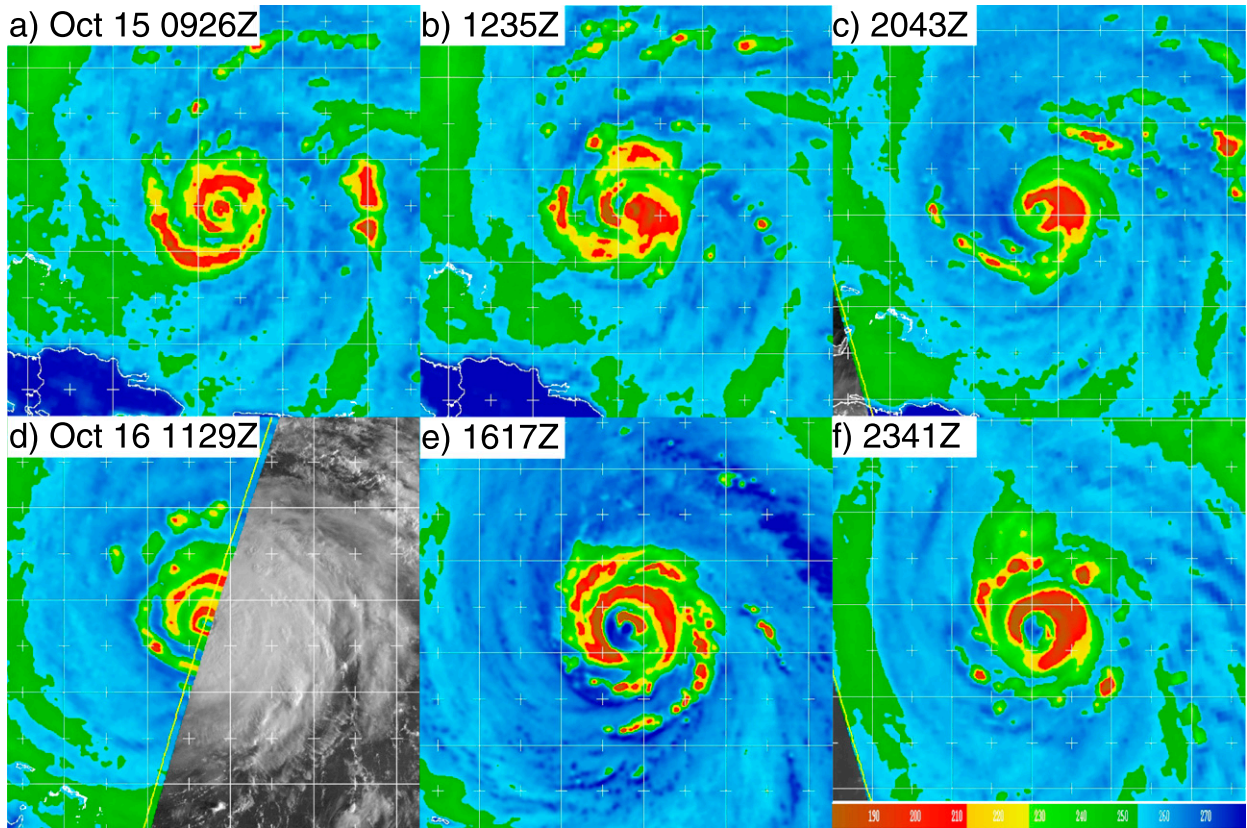
FIG. 2. Microwave imagery of brightness temperatures of Hurricane Gonzalo taken at (a) 0926 UTC 15 Oct, (b) 1235 UTC 15 Oct, (c) 2043 UTC 15 Oct, (d) 1129 UTC 16 Oct, (e) 1617 UTC 16 Oct, and (f) 2341 UTC 16 Oct. All panels except (e) are 91-GHz imagery from the Special Sensor Microwave Imager/Sounder (SSMIS). Panel (e) is 89-GHz imagery from the Advanced Microwave Scanning Radiometer 2 (AMSR2). Images are from the Naval Research Laboratory Monterey Tropical Cyclones webpage (http://www.nrlmry.navy.mil/TC.html).

The analysis of Gonzalo will not be presented in chronological order. Rather, the analysis will be presented in the time relative to the eyewall replacement cycles (ERC relative time). In this approach, we hope to gain a greater understanding of the chronology of the asymmetric structures and processes that are involved. It is apparent that both eyewall replacement cycles had different structures and occurred at different storm intensities. Despite their dissimilarity, we hope to identify common processes that seem fundamental to asymmetric concentric eyewall evolution. In a changing tropical cyclone and particularly during a replacement

cycle, the wind–pressure relationship at each eyewall is a source of uncertainty and an active area of research. But a fundamental, ubiquitous point in time during an eyewall replacement cycle is when the maximum winds of the storm shift from the inner to outer eyewall. Given Gonzalo's evolution, the ERC-relative time will be specified relative to the minimum central pressure for each eyewall replacement cycle. We found that in this pressure-relative time frame, the relative wind speeds at each eyewall progress in the expected fashion. The first two times are named "inner primary 1" and "inner primary 2." These times occur when the maximum

TABLE 1. Details of each aircraft mission selected for the study.

| Time name	Date	Eye-crossing time(s)	ERC-relative time(s)	Aircraft	Radar
Inner primary 1	16 Oct 2014	1117 and 1225 UTC	−0.7 and +0.4 h	N43	TA
Inner primary 2	15 Oct 2014	1445 UTC	+2.8 h	N43	TA
Outer primary 1	16 Oct 2014	1805 and 1827 UTC	+6.1 and +6.5 h	WB-57	HIWRAP
Outer primary 2	15 Oct 2014	2037 and 2116 UTC	+8.6 and +9.3 h	WB-57	HIWRAP
Outer primary 1	16–17 Oct 2014	2251 and 0035 UTC	+10.5 and +12.6 h	C-130	—
Outer primary 2	16 Oct 2014	0042 and 0233 UTC	+12.7 and +14.6 h	C-130	—
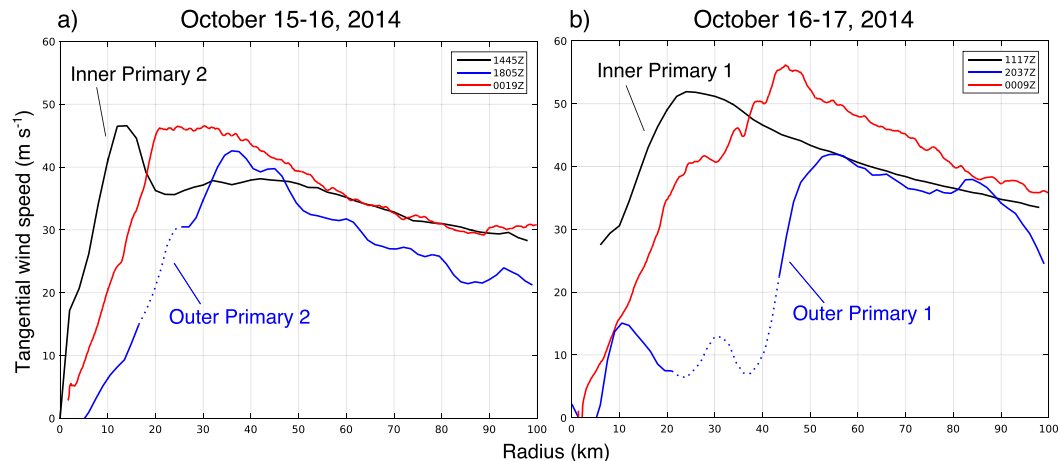
FIG. 3. Azimuthally averaged tangential winds for each aircraft mission. P3 (black) and HIWRAP (blue) winds are averaged over the 2.5–3-km altitudes. USAF (red) flight level winds are at the 700-hPa level. Dotted lines represent locations of large uncertainty in the wind analysis.

winds of the storm are associated with the inner eyewall, making this the primary eyewall of the storm. The second two times are named "outer primary 1" and "outer primary 2," as these occur after the maximum winds shift to the outer eyewall. Table 1 lists these ERC-relative times for each mission.

4. Analysis of inner primary 1

The inner primary 1 time of the ERC-relative framework spans from −0.7- to 0.4-h relative to the minimum central pressure of the second eyewall replacement cycle. This event was also Gonzalo's minimum pressure and maximum intensity. Figure 4 shows the 2-km TA radar reflectivity and the lower fuselage (LF) radar reflectivity from the two NOAA P3 passes. The TA radar reflectivity overviews the data coverage used for the kinematic analysis, and the LF radar reflectivity shows the inner-core precipitation features at higher resolution.

The eyewall has an asymmetric structure with discontinuous stretches of reflectivity that make up the convective ring. The heaviest precipitation falls in the northern half of the eyewall, which, relative to the wind shear vector, is mostly the left-of-shear half. The weakest precipitation occurs in the right-of-shear half, which is open to the southeast. This asymmetry is consistent with the composite studies done by Chen et al. (2006) and Hence and Houze (2011), where the highest eyewall reflectivity regularly occurred in the left-of-shear half of the storm. Other modeling and observational studies found this same reflectivity asymmetry (e.g., Black et al. 2002; Rogers et al. 2003; Reasor et al. 2013). The fragmentation of the eyewall is reminiscent of observed polygonal eyewalls (Kossin and Schubert

2001). Braun et al. (2006) and Reasor et al. (2009) attributed the distorted polygonal reflectivity structure to mesovortices embedded within the eyewall.

Outside of the eyewall, the developing outer eyewall consists of disconnected and loosely organized rainbands. There was a precipitation-free moat region occurring in the southeast at 1117 UTC and in the southwest at 1225 UTC. An azimuthal average (not shown) shows that the rainbands consolidate into a broad secondary reflectivity maximum, indicating a developing outer eyewall. This region encompasses a weak in–up–out overturning circulation, but there is no secondary tangential wind maximum (Fig. 3).

Figure 5 presents the TA radar average cross sections of the four quadrants relative to the wind shear vector, which had a magnitude of $6.6 \, \mathrm{m \, s^{-1}}$ at this time. Data from 1117 and 1225 UTC were merged to calculate the quadrant averages. The downshear-right (DR) quadrant shows a distorted, relatively weak inner eyewall reflectivity tower. A layer of radial inflow extends into the inner eyewall. It then turns upward and outward, completing an in–up–out overturning circulation. Traveling downwind to the downshear-left (DL) quadrant, radial inflow is at its deepest and strongest. This inflow begins a pronounced in–up–out overturning circulation that feeds a well-defined reflectivity tower of the inner eyewall. The updraft here reaches over $8 \, \mathrm{m \, s^{-1}}$ at 8-km altitude. Below 2-km altitude, radial convergence is apparent at 60–70-km radius, which likely indicates the dynamical organization of the developing outer eyewall.

In the upshear-left (UL) quadrant, the inner eyewall continues to exhibit a prominent reflectivity tower. However, this tower is surrounded by radial inflow and descent, opposite to the flow pattern of that seen in the DR
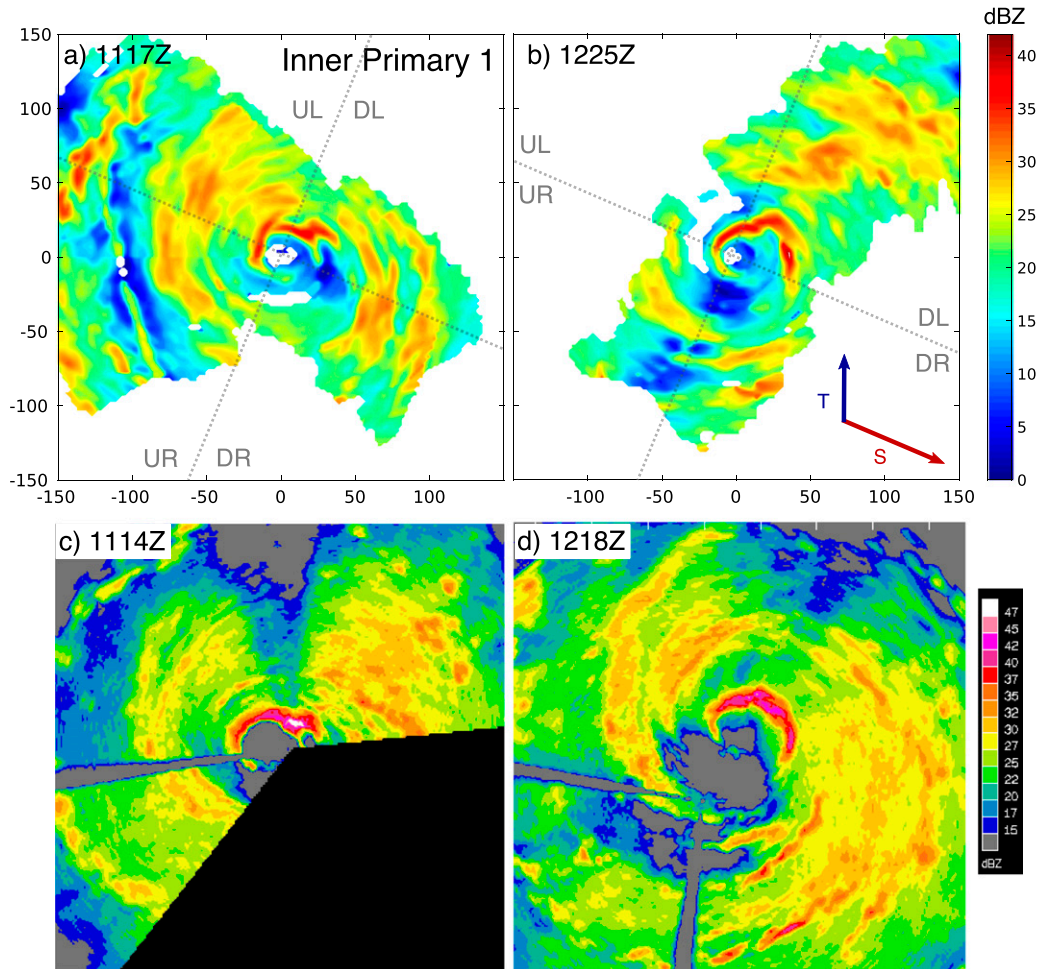
FIG. 4. TA radar 2-km reflectivity for the inner primary 1 analysis time, which is at (a) 1117 and (b) 1225 UTC 16 Oct. Both axes display distance (km) from the storm center. Vectors for the storm track (*T*) and environmental wind shear (*S*) are shown. The storm track and shear magnitudes are 4 and 6.6 m s^{-1}, respectively. LF radar reflectivity is also shown at (c) 1114 and (d) 1218 UTC 16 Oct.

quadrant. At the outer eyewall, radial inflow below 1-km altitude appears to overturn into radial outflow just above the 1-km level. This sharp overturning is similar to that seen in the mature outer eyewall of Hurricane Rita from Didlake and Houze (2011). They found that the outer eyewall overturning signature was indicative of enhanced supergradient boundary layer flow. In the upshear-right (UR) quadrant, neither eyewall radius contains any clear overturning flow to feed convection.

The eyewall wavenumber-1 asymmetry alignment with the wind shear is well studied. It is generally attributed to two dynamical processes that may not be mutually exclusive: 1) a thermal balance response to the shear-induced vortex tilt (Jones 1995; Frank and Ritchie 1999; Reasor and Eastin 2012), and 2) a dynamic balanced response of vertical motion from differential vorticity advection (Bender 1997; Frank and Ritchie 1999, 2001; Wu et al.

2006). Additionally, mesovortices that interact with the low-level flow also contribute to the asymmetry (Braun et al. 2006). The overall quadrant asymmetry pattern of the primary eyewall has some consistencies with the composite analyses of DeHart et al. (2014) and Zhang et al. (2013). Using P3 TA radar and dropsonde observations, these studies found that the strongest low-level inflow and eyewall updrafts occurred in the downshear quadrants.

The wavenumber-1 structure of developing outer eyewalls has not been studied as much as that of inner eyewalls. At the inner primary 1 time, the outer eyewall does have distinct variations around the storm and appears similar to the inner eyewall. Both DR and DL quadrants have an in–up–out overturning circulation at both eyewalls. But in the UL quadrant, the two eyewalls have different transverse circulation patterns. With slight upward motion still occurring at the outer eyewall in the UL
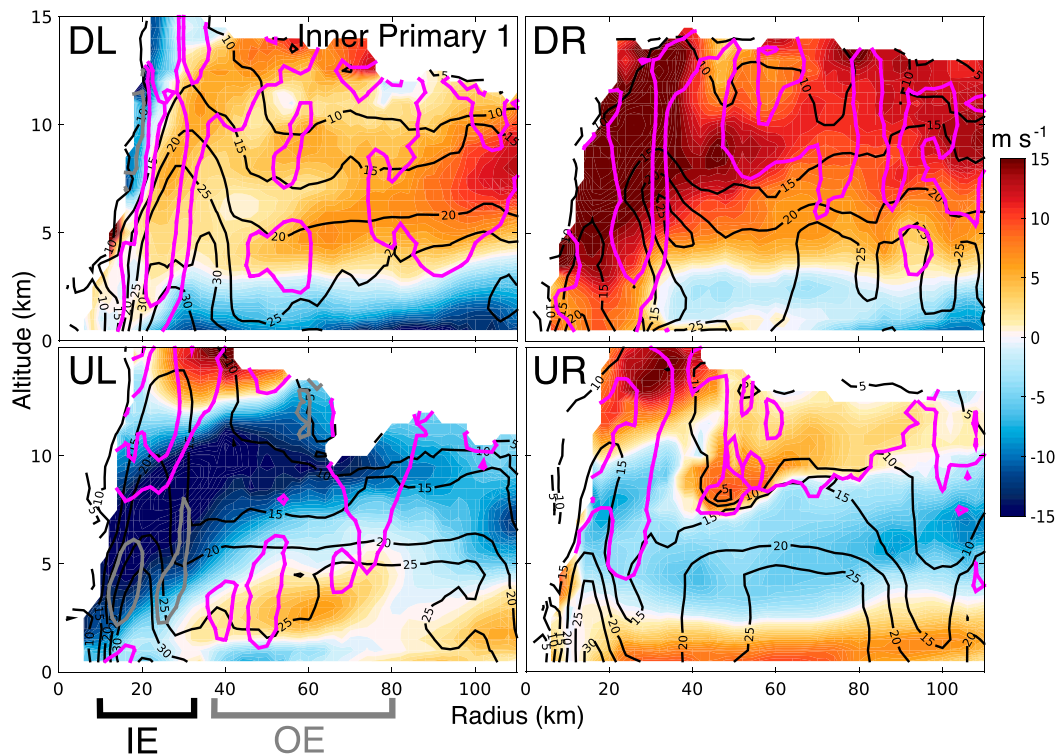
FIG. 5. Averaged vertical cross sections of winds and reflectivity for the wind shear–relative quadrants [downshear-left (DL), downshear-right (DR), upshear-left (UL), and upshear-right (UR)] at the inner primary 1 analysis time. Radial velocity is shown in the filled contours, where negative values indicate flow toward the storm center. Reflectivity contours (dBZ) are in black. Vertical velocity is shown in pink and gray contours. Upward motion (pink) is contoured at $+1$ and $+3\,\mathrm{m\,s^{-1}}$, and downward motion (gray) is contoured at -1 and $-3\,\mathrm{m\,s^{-1}}$. Approximate radial ranges of the inner eyewall (IE) and outer eyewall (OE) are marked.

quadrant, the in–up–out circulation here extends farther downwind of that in the inner eyewall. The reflectivity pattern in Fig. 4d supports the observed kinematics. A broad region of reflectivities $>30\,\mathrm{dB}Z$ in the developing outer eyewall occurs slightly more downwind than the high reflectivities of the inner eyewall. This finding is consistent with TRMM Precipitation Radar observations of storms with concentric eyewalls (Hence and Houze 2012a).

The evolution of the transverse circulation is intimately tied to the evolution of the tangential wind circulation. Understanding this interaction is essential for explaining ERC evolution. To investigate these dynamics, we calculate certain terms from the tangential momentum equation in cylindrical coordinates (r, θ, z), which is given by

$$\frac{\partial v}{\partial t} = -u\eta - \frac{v}{r}\frac{\partial v}{\partial \theta} - w\frac{\partial v}{\partial z} - \frac{1}{\rho}\frac{\partial p}{\partial \theta} + F_\theta, \qquad (1)$$

where

$$\eta = \frac{\partial v}{\partial r} + \frac{v}{r} + f. \qquad (2)$$

In these equations, u, v, and w are the radial, tangential, and vertical velocities, respectively; p is pressure; ρ is density; and f is the Coriolis parameter. We call the $-u\eta$ term the generalized Coriolis force (Smith et al. 2009; Gu et al. 2016). The other right-hand-side terms are azimuthal advection, vertical advection, pressure gradient acceleration, and dissipation. We recognize that the dissipation term cannot be neglected within the boundary layer, but we cannot estimate it with the given data, nor can we estimate the pressure gradient term. Thus, we focus on the first three terms in the current analysis, and we refer to these as the advective tendency terms.

Figure 6 shows the sum of the advective tendency terms between 0- and 2-km altitude across all azimuths from the TA radar. Just as in the transverse circulation from Fig. 5, the advective tendency terms have an apparent wavenumber-1 asymmetry. Negative advective tendency is most prominent in the right-of-shear quadrants, while positive advective tendency is most prominent in the left-of-shear quadrants. The largest positive magnitudes occur slightly inward of the radius of maximum wind in the inner eyewall. This inward
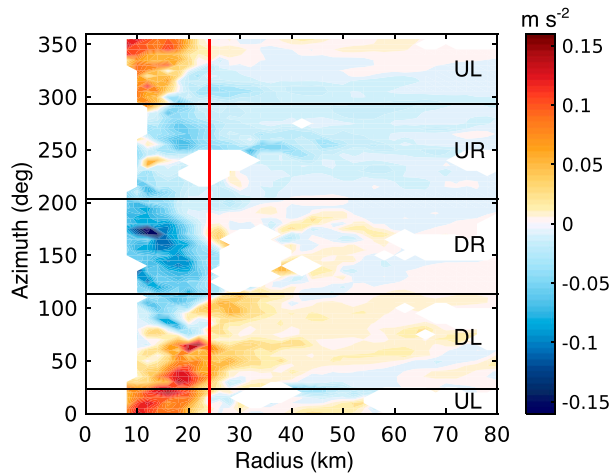
FIG. 6. Sum of tangential momentum advective tendency terms over selected radii and all azimuths at the inner primary 1 analysis time. Values are averaged terms between 0- and 2-km altitude. The red vertical line marks the radius of maximum axisymmetric tangential wind in the same altitudinal average. The plot is divided into the shear-relative quadrants.

displacement of positive advective tendency is apparent in the axisymmetric analysis (not shown) and is consistent with a contracting eyewall (Shapiro and Willoughby 1982). The generalized Coriolis term dominates the positive advective tendency signal in the DL and UL quadrants due to the strong radial inflow (Fig. 5). A closer look at Fig. 5 (DL and UL) shows that the radial inflow below 2 km and at the inner eyewall radius comes from the two distinct flow patterns. The boundary layer inflow forces the positive advective tendency in the DL quadrant. In the UL quadrant, midlevel inflow from outside the eyewall descends and joins the low-level inflow to contribute to the corresponding positive advective tendency. This modification of the low-level inflow is also marked by a shift in the radius of maximum advective tendency from ~18-km radius in the DL to 8–12-km radius in the UL. As shown in Fig. 5, low-level radial inflow still contributes to the UL positive advective tendency, but not as a connected inflow layer. The developing outer eyewall marks the break in radial inflow, suggesting that this flow pattern actively inhibits some low-level inflow from reaching the inner eyewall. Outside of the inner eyewall, advective tendency is weaker but prominently positive within the DL quadrant.

5. Analysis of inner primary 2

The inner primary 2 time of the ERC-relative timeline occurs approximately 2.8 h after Gonzalo reached its minimum central pressure during the first eyewall replacement
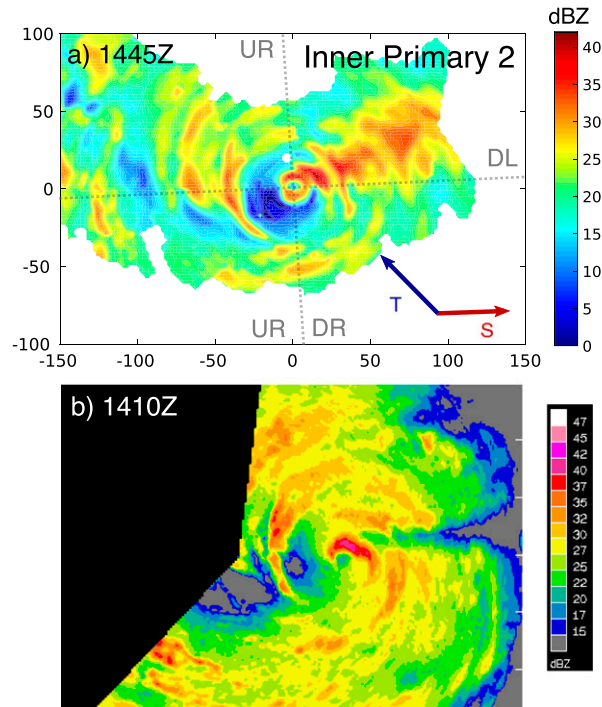

FIG. 7. As in Fig. 4, but with TA radar data for inner primary 2. The storm track and shear magnitudes are 5 and 4.4 m s^{-1}, respectively.

cycle on 15 October. Compared to inner primary 1, these observations show Gonzalo when it was weaker. Yet, for inner primary 2, the observed structures indicate changes that may be representative of eyewall replacement cycle evolution. In Fig. 7a, the 2-km reflectivity shows asymmetric inner and outer eyewalls, and the moat between. The heaviest precipitation of the inner eyewall is located in the DL quadrant of the storm, exhibiting a similar distribution to the precipitation asymmetries observed in past studies (Black et al. 2002; Hence and Houze 2011; Reasor et al. 2013). The developing outer eyewall is disconnected and loosely organized, but it appears as a reflectivity maximum in an axisymmetric average (not shown). Both eyewalls contain axisymmetric tangential wind maxima, but the inner eyewall winds remain the strongest.

The quadrant analysis presented in Fig. 8 has patterns similar to inner primary 1 but with a notable upwind shift. The DR quadrant has deep radial inflow that extends to the primary eyewall. This flow turns upward into the strongest updraft in the storm, consistent with past studies (DeHart et al. 2014; Braun et al. 2006; Corbosiero and Molinari 2002, 2003). An in–up–out overturning circulation also occurs at the outer eyewall.

Downwind in the DL quadrant, the low-level inflow is shallower. At the inner eyewall, low-level inflow is weaker than in the DR quadrant, and even turns into weak outflow. The inner eyewall is dominated by sinking
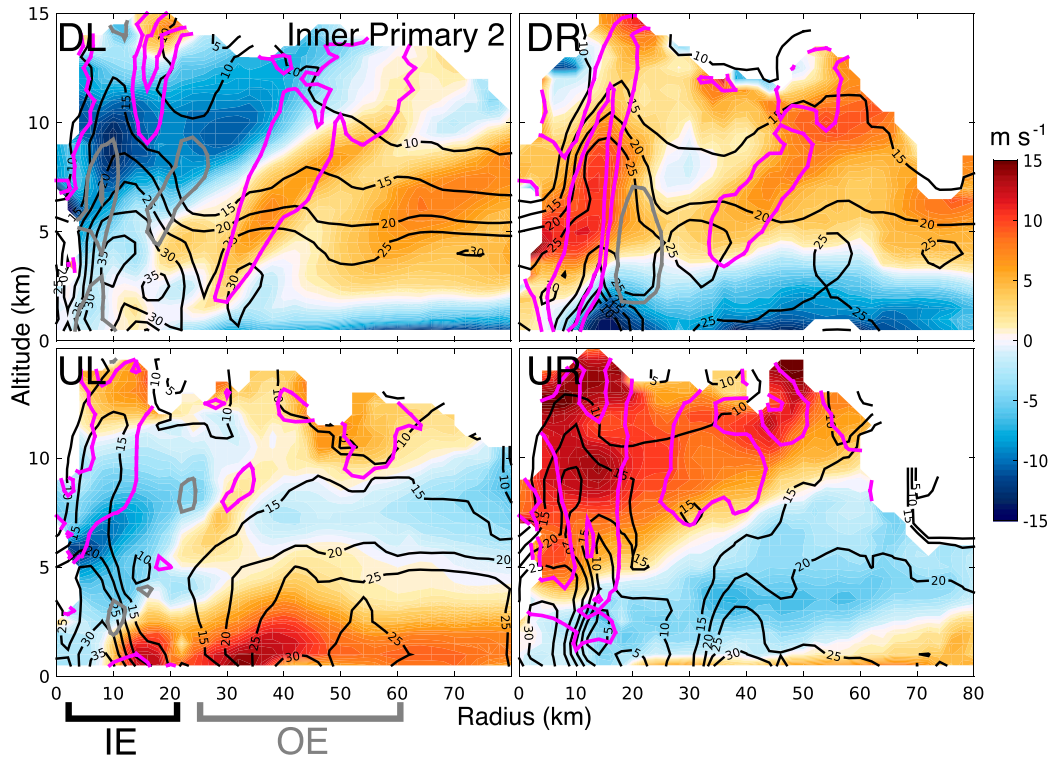
FIG. 8. As in Fig. 5, but with TA radar data for inner primary 2. Upward motion (pink) is contoured at +2 and +4 m s^{-1}, and downward motion (gray) is contoured at −1 and −3 m s^{-1}.

inflow throughout most of the troposphere, opposite to the flow in the DR quadrant. The outer eyewall still exhibits an in–up–out circulation. As in inner primary 1, the outer eyewall overturning circulation remains vigorous farther downwind than the inner eyewall overturning circulation. Figure 7b supports the observed kinematics as an outer eyewall band has intense convection farther downwind than that of the inner eyewall. Neither of the upshear quadrants exhibits an in–up–out circulation at either eyewall.

The advective tendency terms from Eq. (1) explain the asymmetric evolution of the v field (Fig. 9). As in inner primary 1 (Fig. 6), a maximum of advective tendency occurs radially inside the radius of maximum wind at the inner eyewall. Here, the maximum occurs at the boundary between the UR and DR quadrants. It indicates an upwind shift of the circulation asymmetry in Fig. 8. The inner eyewall again has two distinct regions of positive advective tendency. One such region from 210° to 100° is a result of the boundary layer inflow, which is associated with inner eyewall contraction. Outside of the inner eyewall, positive advective tendency extends farther from the center where the tangential winds of the outer eyewall are being strengthened largely in the DR quadrant where data are available. Between 130° and 70°, the inner extent of positive advective tendency produced

by low-level inflow moves away from the center. Farther downwind, remnants of slightly positive advective tendency exist between 70° and 40° outside of the radius of maximum wind, which is consistent with the remaining low-level inflow. This pattern of positive advective tendency and the pattern of low-level radial inflow in Fig. 8 (DL quadrant) again suggest that the outer eyewall
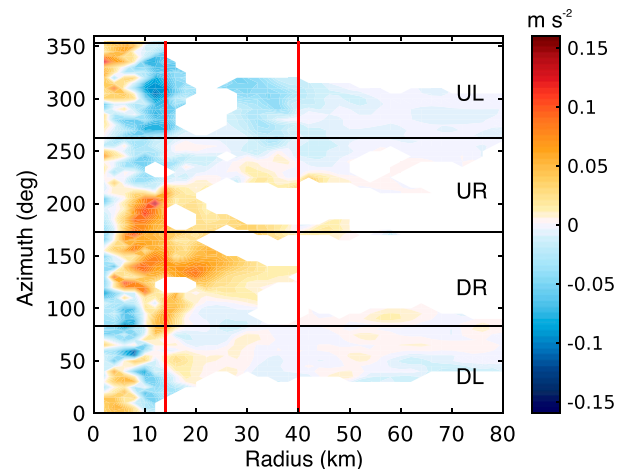

FIG. 9. As in Fig. 6, but with TA radar data for inner primary 2. The second red vertical line is the radius of secondary maximum axisymmetric tangential wind associated with the outer eyewall.
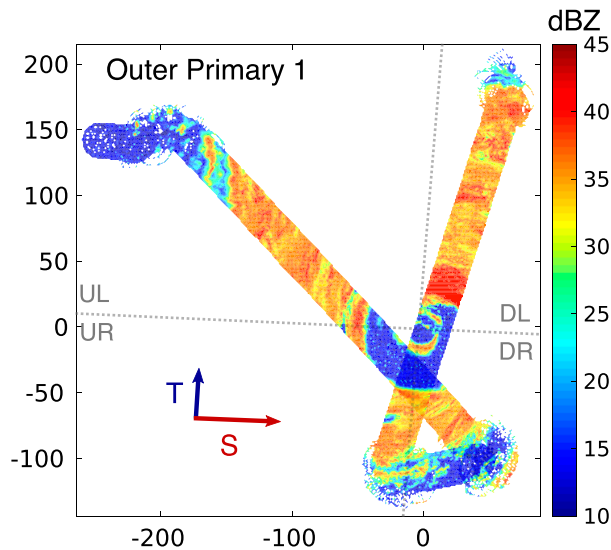
FIG. 10. HIWRAP radar 2-km reflectivity at the outer primary 1 analysis time (see Table 1). Vectors for the storm track (*T*) and environmental wind shear (*S*) are shown. The storm track and shear magnitudes are 3 and 5.2 m s^{-1}, respectively. Both axes display distance (km) from the storm center.

prevents some radial inflow from reaching the inner eyewall at these downwind azimuths, limiting its convection and low-level tangential wind acceleration.

6. Analysis of outer primary 1

The observations for outer primary 1 and 2 times are from the HIWRAP radar. Figure 10 shows the 2-km-level HIWRAP reflectivity for outer primary 1, which occurs at +6.1 h (northeast–southwest pass) and +6.7 h (southeast–northwest pass) in the ERC-relative time frame. Compared to the P3 TA radar, the HIWRAP radar covers a narrower region, reaching 30 km in width at the surface. Although the southeast–northwest pass did not pass directly over the storm center, the concentric eyewall pattern is still evident in the observations. The outer eyewall appears very broad in the northeast, as it extends into the moat region and possibly connects with the inner eyewall. Simultaneously in this region, the inner eyewall has noticeable breaks in its ring pattern. At this time, the maximum winds in the storm have switched from the inner to the outer eyewall (Fig. 3). As also suggested by the reflectivity structure, this switch means that the inner eyewall has begun to decay.

Figure 11 presents reflectivity and retrieved winds along each flight pass from outer primary 1. Guimond et al. (2016) demonstrated the wind retrieval accuracy from HIWRAP observations by comparing to TA radar data in the inner core of Hurricane Karl (2010). Based on the error analyses from Guimond et al. (2014), the

errors for the retrieved winds were 0.2, 2.5, and 0.25 m s^{-1} for the radial, tangential, and vertical winds, respectively, on most overpasses. The low radial and vertical velocity errors relative to the retrieved velocity magnitudes indicate good accuracy of the retrieved HIWRAP wind fields. The off-centered overpass in outer primary 1 resulted in slightly larger errors in the retrieved horizontal winds: 2.5 m s^{-1} for both radial and tangential winds. These errors did not impact the overall conclusions of this study.

The shear vector was pointed eastward (94°) at the outer primary 1 time. With the narrowness of the HIWRAP swath, the data coverage in each shear quadrant is much smaller than the TA radar observations. The azimuthal coverage of the HIWRAP swath at 2-km altitude is 44° at 20-km radius and 8° at 100-km radius, which are both much less than a 90° quadrant. We therefore present the HIWRAP observations not as quadrant composites, but rather as cross sections of the wind and reflectivity fields at specific azimuths within each quadrant. For passes that are misaligned with the storm center, the specified azimuth is calculated by averaging all azimuths covered by the cross section within 100-km radius.

Despite the limited coverage of each quadrant, the analyses of outer primary 1 in Fig. 11 present notable differences among the cross sections, consistent with the TA radar data of earlier times. The DR cross section shows distinct reflectivity towers in the inner and outer eyewalls. Both eyewalls are dominated by radial inflow that extends upward to the midtroposphere, with outflow dominant just above. For the inner eyewall, the radial inflow coincides with sinking motion. In the previous times, this quadrant exhibited a well-defined in–up–out circulation pattern. Here, this expected pattern is absent, possibly because of the decay of the inner eyewall. In the outer eyewall, there is slight ascent throughout the reflectivity tower, providing a more defined in–up–out circulation pattern.

In the DL cross section, the outer eyewall overturning circulation is also apparent, but it is much shallower. Between 30- and 50-km radius, radial inflow occurs only below 1-km altitude, while the maximum outflow from the outer eyewall begins around 2-km altitude. The shallower outer eyewall inflow and outflow layers between the DR and DL quadrants are consistent with the earlier times. On the other hand, the inner eyewall radii (5–20-km radius as seen in the DR and UR cross sections) have a clear in–down–out circulation, which again is not conducive for convection. Downwind, the UL cross section only has data from the outer eyewall due to the off-centered overpass. In the outer eyewall, there is shallow radial inflow that turns into upward motion
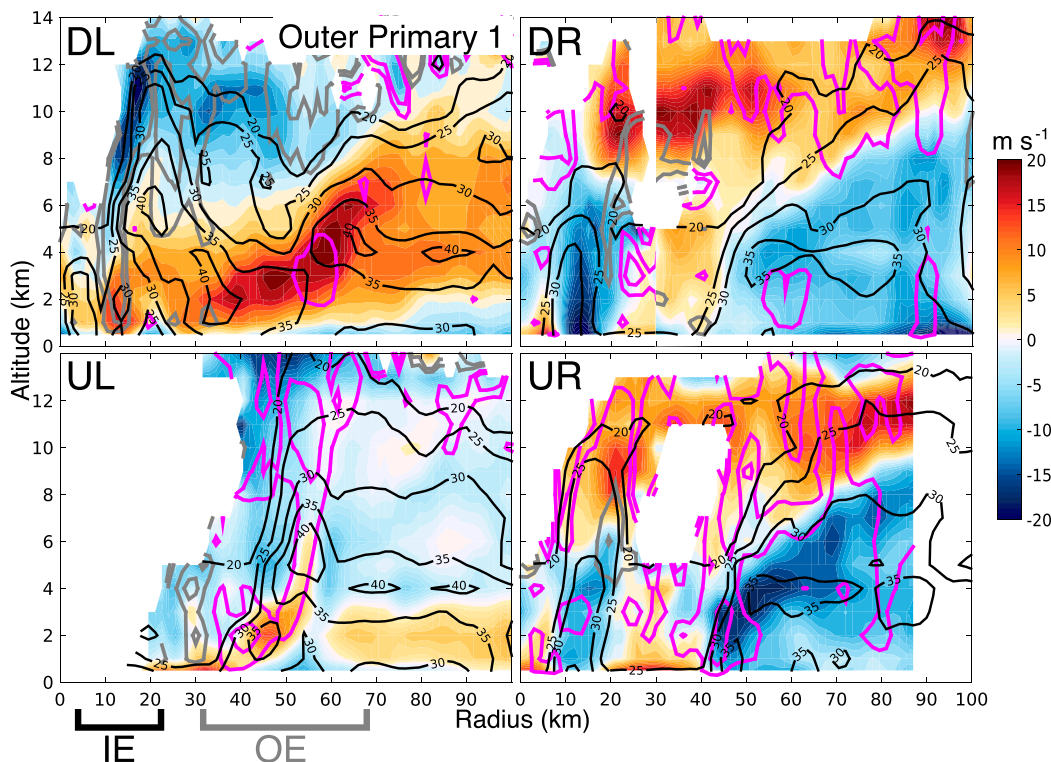
FIG. 11. Vertical cross sections of winds and reflectivity in the wind shear–relative quadrants at the outer primary 1 analysis time. Cross sections are along selected azimuths 20° (DL), 151° (DR), 292° (UL), and 194° (UR). Radial velocity where negative values indicate flow toward the storm center. Reflectivity contours are in black. Vertical velocity is shown in pink and gray contours. Upward motion (pink) is contoured at +3 and +6 m s^{-1}, and downward motion (gray) is contoured at −3 and −6 m s^{-1}.

within a narrow channel along the inner edge of the reflectivity tower. The UR pattern is very similar to the DR since the cross-section azimuths are separated by only 43°. These cross sections are from the southern segments of the two overpasses in Fig. 10.

Given the limited coverage of HIWRAP's narrow swath, there still remains uncertainty about Gonzalo's asymmetry. To further verify this asymmetric kinematic structure, we compare the radar observations to flight-level observations. Although the C-130 flights examined herein were not coincident with the WB-57 flights, we expect that the wavenumber-1 structural changes would occur more slowly than the flight mission frequency, which would result in some consistency seen in the observations.

Figures 12a and 12c show flight-level radial and tangential winds collected 5–7 h after the outer primary 1 time. Each leg exhibits a single tangential wind maximum between 35- and 45-km radius along with a nearby maximum in radial outflow, which is part of the eyewall overturning circulation. Radially outside of this maximum in the UR leg, radial flow alternates between inflow and outflow, which is unlike the steady, strong

inflow seen at the 3-km level in the UR HIWRAP cross section (Fig. 11). The flight-level DR leg is more like that of the HIWRAP data, as it predominantly exhibits radial inflow outside of 50-km radius. The DL leg has both the strongest radial outflow and inflow. The outflow peak near 45-km radius is consistent with the HIWRAP data at this altitude, while the inflow peak near 70-km radius is not consistent. Last, the UL leg outside of 45-km radius is consistent with the HIWRAP data, showing predominant radial outflow not seen in the other quadrants.

The discrepancies between the flight-level and HIWRAP data possibly occur because of the different azimuths of the flight legs, or because of small-scale kinematic fluctuations occurring within the hours separating the two flights. But several similarities, including strongest outflow in the DL, predominant outflow in the UL, and predominant inflow in the DR, strongly support the existence of the wavenumber-1 asymmetry gleaned from the HIWRAP data.

The HIWRAP observations detail vertical wind, radial wind, and reflectivity structures consistent with expectations. Still, there were some limitations that do not
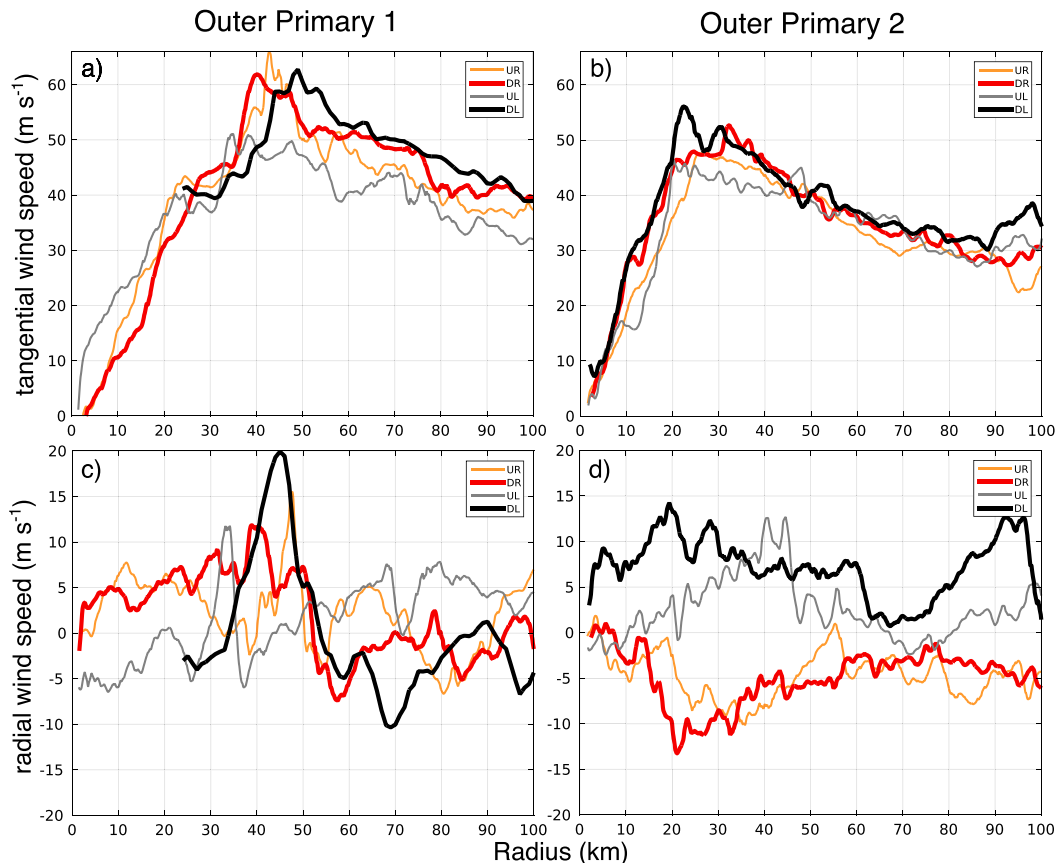
FIG. 12. USAF 700-hPa winds for the outer primary times. Tangential winds within each shear-relative quadrant are shown for (a) outer primary 1 and (b) outer primary 2. Radial winds are also shown for (c) outer primary 1 and (d) outer primary 2.

allow for a calculation of tangential momentum budget. Didlake et al. (2015) demonstrated that with the HIWRAP scanning geometry, the cross-track component of the wind is the least accurately retrieved. Here, the cross-track component is largely the tangential wind. Thus, the derivative terms necessary for calculating the tangential momentum budget were especially difficult to produce. Gonzalo's moat on 16 October had so few scatterers that the HIWRAP Doppler velocity observations were particularly noisy. This noise degraded the wind retrieval along the outer eyewall inner edge, particularly for the tangential wind. The second issue is that the Ku- and Ka-band beams were attenuated in the heavy eyewall precipitation on 15 October. This attenuation negatively impacts the raw Doppler signal, particularly in the low levels where the winds are strongest. As a result, the retrieved tangential winds were again most degraded.

Despite these negative impacts, we assume that the pattern of advective tendency follows that of the radial and vertical wind components below 2-km altitude. In

the TA radar data, there was an apparent correlation between the u, w terms and the generalized Coriolis force, vertical advection terms at altitudes below 2 km. Radial inflow and upward motion mostly corresponded with positive advective tendency, and the magnitude of the generalized Coriolis term was much greater than that of the vertical advection term. Gu et al. (2016) demonstrated this relationship between the low-level generalized Coriolis force and low-level radial flow, yet they found the opposite relationship with vertical motion and vertical advection. This opposite relationship is likely due to the fact that they focused on a layer (1.6-km altitude and below) where v is increasing with height. Here we focus on a slightly higher layer (2 km and below), which includes decreases in v with height. Given this reasoning, we speculate that the largest advective tendency in the outer eyewall occurs in the DR and UR cross sections where substantial radial inflow coincides with persistent upward motion below 2 km. The tangential wind strengthening in the DR cross section is consistent with the inner eyewall asymmetry from inner
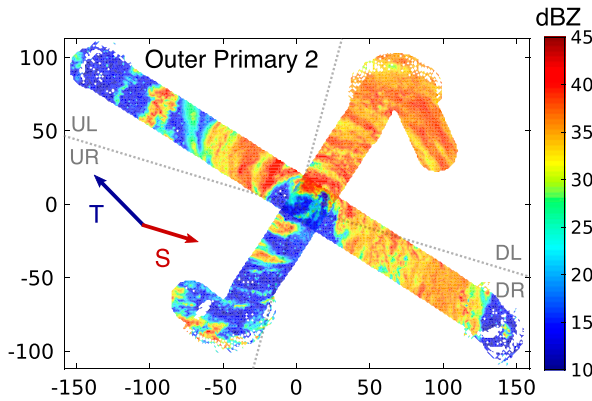
FIG. 13. As in Fig. 10, but with HIWRAP data for outer primary 2. The storm track and shear magnitudes are 5 m s^{-1} and 4.2 m s^{-1}, respectively.

primary 2. This connection highlights how the outer eyewall is developing features that are expected of the primary eyewall in a storm.

7. Analysis of outer primary 2

The final time in this ERC-relative analysis occurs at 8.6 h (southwest–northeast pass) and 9.3 h (southeast–northwest pass) past the minimum pressure of the replacement cycle. As seen in Fig. 13, outer primary 2 encompasses two nearly perpendicular passes over Gonzalo's inner core. The inner eyewall appears as a broken ring of convection with substantial openings to the northwest and southeast of the center. This reflectivity pattern depicts a decaying inner eyewall. Just outside, the outer eyewall also does not appear as a connected reflectivity ring, with an opening in the south-southwest. This discontinuity differs from the outer eyewall in outer primary 1, which may also just reflect the fact that the storm is slightly less intense here in the outer primary 2 time.

Figure 14 shows the HIWRAP cross sections in each shear quadrant. In the DR cross section, the radial inflow layer has a depth of nearly 4 km. Heavy precipitation is widespread throughout the cross section, but at 10–35-km radius, the heaviest precipitation attenuates both the Ku and Ka beams of HIWRAP. As a result, accurate measurements of reflectivity and velocity were not possible below ~3-km altitude in this region. The outer eyewall occurs in this region between 25- and 30-km radius, as there is a channel of rising outflow extending above 8-km altitude.

The DL cross section also has widespread heavy precipitation, but the attenuated region (near 30-km radius) is notably smaller than in the DR cross section. The radial inflow layer is shallower, but the airflow still

turns upward into a strong updraft between 25- and 35-km radius. With such prominent radial inflow and upward motion, both DR and DL cross sections have wind patterns consistent with positive advective tendency at the outer eyewall radius, where the DR tangential wind advection is likely the greater of the two. Both DR and DL cross sections exhibit shallow updrafts at 5–10-km radius, possibly associated with the decaying inner eyewall. The outer eyewall in the UL cross section largely displays an in–down–out pattern similar to that seen in the upshear quadrants of the inner primary times.

The UR cross section shows two reflectivity towers extending to 5-km altitude, which are the outer and inner eyewalls. Although the inner eyewall overall is decaying at this stage of the eyewall replacement cycle, it retains a reflectivity tower in this quadrant. Outward-sloping updrafts occur above both towers. They coincide with a maximum in reflectivity between 6- and 11-km altitude, which indicates a large amount of ice and its convection appears separate from the shallow reflectivity towers. The upper-level reflectivity and w maxima are consistent with past studies that highlight enhanced upward motion and ice at the upper levels of the eyewall (Lord et al. 1984; Black et al. 1996; Braun 2002; Zipser 2003; Fierro et al. 2009). At this altitude, latent heat of fusion and decreased amounts of heavy hydrometeors increase the upper-level buoyancy. A 45 m s^{-1} tangential wind maximum also occurs here at 8-km altitude (not shown).

Figures 12b and 12d present flight-level data collected 3–5 h after the outer primary 2 time. The observed radial velocities are largely consistent with the 3-km level HIWRAP data (Fig. 14) and confirm the same wavenumber-1 structure in outer primary 2. Radial inflow is predominant in the right-of-shear legs, while radial outflow is predominant in the left-of-shear legs.

Figure 15 shows radial profiles of the u, v, and w HIWRAP winds averaged below 2 km for all ERC times and shear quadrants. At outer primary 2, the inner eyewall in the UR cross section has a reflectivity tower (Fig. 14d) and a local tangential wind maximum (Fig. 15) that are not found in the other quadrants at this time. When compared to outer primary 1, two additional cross sections (DL and DR) exhibited distinct inner eyewall tangential wind and reflectivity features. But at this later time in the ERC-relative framework, the inner eyewall in all cross sections but the UR has weakened considerably if not completely dissipated. The shallow updrafts of the decaying inner eyewall in the DL and DR cross sections of outer primary 2 are not associated with tangential wind or reflectivity features. Such an asymmetric dissipation would have ramifications on the overall intensity, as the vortex adjusts to the mixing of the older
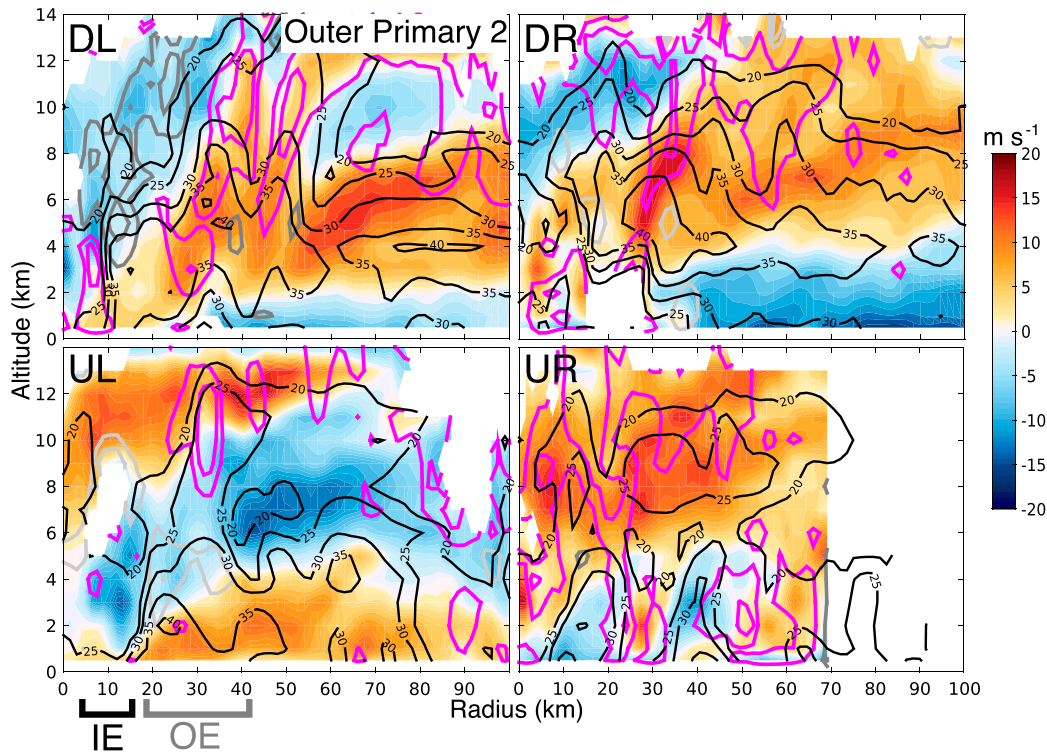
FIG. 14. As in Fig. 11, but with HIWRAP data for outer primary 2. Cross sections are along selected azimuths 36°
(DL), 117° (DR), 307° (UL), and 206° (UR).

eye air mass with the newer eye air mass (Zhu et al. 2004; Chen et al. 2011; Sitkowski et al. 2012).

8. Discussion

a. Azimuthal upwind shift

The maximum axisymmetric tangential winds in Gonzalo switched locations from the inner eyewall at the early times (inner primary 1, 2) to the outer eyewall at the late times (outer primary 1, 2). Along with this switch, the observations also hint at an azimuthal shift in the kinematic structure of the concentric eyewalls between the inner and outer primary times. To highlight this shift, we closely examine the radial profiles of Fig. 15.

For each time, the two quadrants that have the largest radial inflow at both eyewalls are marked with the letters A (at the inner eyewall) and B (at the outer eyewall). The two quadrants that have the largest updrafts at each eyewall are also marked. Since the inner eyewall was decaying in the outer primary times, we did not mark the maximum inflow and updrafts for the inner eyewall here. Because of low-level attenuation in outer primary 2, we used midlevel values seen in Fig. 14 to select the maximum quadrants; moreover, both inflow and updraft

maxima were located in the DR and DL quadrants at this time.

Next, we highlight in Fig. 15 the locations where both a maximum in inflow and updraft are present at each eyewall. These locations mark the quadrants where an eyewall's overturning circulation, and thus positive tangential wind advection, is strongest. From Fig. 15, the azimuthal upwind shift of maximum overturning circulation, which was hinted in previous sections, is apparent between eyewalls and over time. At the inner primary times, maximum overturning circulation in the outer eyewall spanned the UL and DL quadrants. Concurrently, maximum overturning circulation in the inner eyewall spanned the DL and DR quadrants, indicating an upwind shift from the outer to the inner eyewall. For the outer primary times, maximum overturning in the outer eyewall spanned the DL, DR, and UR quadrants, indicating another upwind shift from the inner primary times.

The azimuthal offset of maximum overturning circulation between the two eyewalls is evident from these observations and requires a dynamical explanation. The inner eyewall has a maximum overturning circulation in the DR and DL quadrants, which agrees with past studies that point to an asymmetric dynamic and
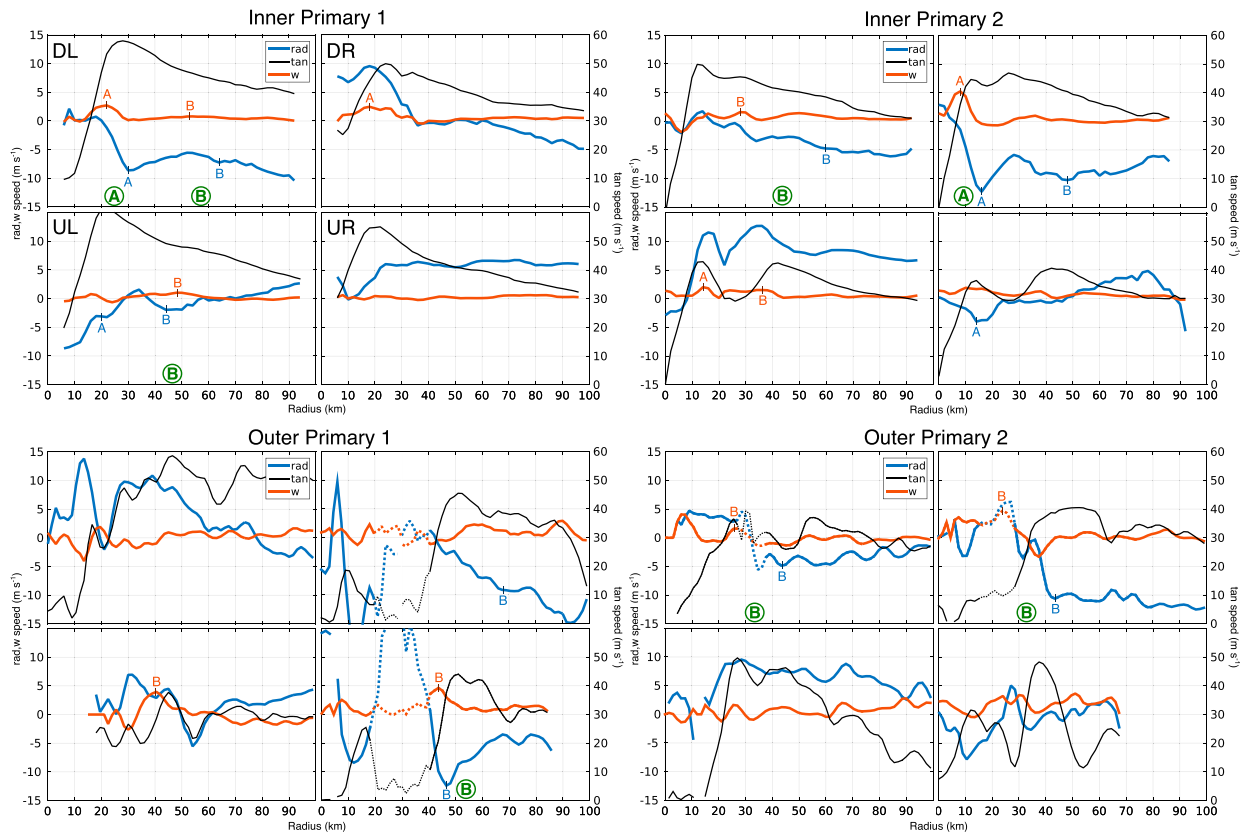
FIG. 15. Radial profiles of the radial, tangential, and vertical velocities for each shear quadrant at each analysis time. Values are averaged over 0–2-km altitude. Inner primary times are TA radar quadrant averages and outer primary times are HIWRAP transects within each quadrant. Dotted lines represent locations of large uncertainty in the wind analysis. The radial velocity profiles are marked with a "B" in the two quadrants where the outer eyewall has the two largest radial inflow speeds (negative radial velocities). The vertical velocity profiles are marked with a "B" in the two quadrants where the outer eyewall has the two largest positive vertical velocities. The same is done for the inner eyewall (marked with an "A") at inner primary times. Green letters mark the eyewall and quadrant where both radial and vertical velocities are marked with "A" or "B."

thermodynamic response to the tilting of the vortex under environmental wind shear (Jones 1995; Bender 1997; Frank and Ritchie 1999, 2001). In a TRMM Precipitation Radar study of TC concentric eyewalls, Hence and Houze (2012a) found that the maximum reflectivity of the outer eyewall occurred downwind of the inner eyewall. The current observations support these previous findings as they highlight the necessary kinematic flow for the asymmetric precipitation pattern in the outer eyewall. However, the dynamics underlying this asymmetric alignment are not clear, particularly when considering past studies.

The vortex tilt yields enhanced inner eyewall convection primarily in the DR and DL quadrants (e.g., Reasor et al. 2013). Riemer et al. (2010) showed that the vortex tilt also leads to convective rainband activity preferentially occurring in the DR and UR quadrants, which is consistent with other rainband studies (Hence and Houze 2012b; Didlake and Houze 2013a,b). If the

pattern of the outer eyewall is consistent with the tilt-induced convection asymmetry, we would expect the preferred region of active convection to fall somewhere between (i.e., upwind of the convective inner eyewall and downwind of the convective rainbands). But this shift is not what occurs in the current observations or past studies, thus the same tilt dynamics may not be the dominant cause for the outer eyewall asymmetry.

One possible explanation for the outer eyewall asymmetry could involve interaction with the dynamics of the rainband complex. During the formation of an outer eyewall, extensive rainband activity is often organized into a near-stationary spiral complex, which would be just radially outside or even merging with the developing outer eyewall (Willoughby et al. 1984). It is possible that the kinematics of the rainband complex as it merges with the outer eyewall are connected to the eyewall asymmetry; however, further study is needed to confirm this connection. We speculate that the

subsequent upwind shift of the outer eyewall asymmetry occurs as it becomes the primary eyewall of the storm, and thereby directly interacts with the environmental wind shear in the expected manner like the earlier inner eyewall.

b. Inner eyewall decay

We have postulated in the current study that at the outer primary times, the inner eyewall decays in large part due to the outer eyewall obstructing low-level moist radial inflow from reaching the inner eyewall and thus reducing its tangential wind acceleration and convection. This barrier effect argued by Samsury and Zipser (1995) is in contrast to other weakening effects that counteract the inner eyewall transverse circulation at higher altitudes (Willoughby et al. 1982; Willoughby 1988; Rozoff et al. 2008). The asymmetric analyses in the inner primary times show that low-level radial flow into the outer eyewall occurs over a larger azimuthal span than the inner eyewall. In the downwind end of this azimuthal span, radial inflow is reduced or even turns outward between the two eyewalls. In either case, the observations suggest the outer eyewall reduces the flow of inward-spiraling low-level air that reaches the inner eyewall.

Several studies found that outer rainbands act as a similar barrier to low-level inflow, where low-level high-θ_e air turns upward at the rainband axis, and midlevel inflow descends bringing low-θ_e air into the boundary layer on the radially inward side (Barnes et al. 1983; Powell 1990a,b; Hence and Houze 2008; Didlake and Houze 2009). Powell (1990a,b) found that these rainbands could reduce θ_e by as much as 20°C. Riemer et al. (2010) and Riemer (2016) found that the boundary layer air that reaches the eyewall does not fully recover from this θ_e reduction, which limits the intensification of the eyewall. While these studies attribute intensity modification to rainband downdrafts, the current observations do not have similar downdraft circulations in the maturing outer eyewall. Midlevel inflow that descends from precipitation loading is not apparent in the outer eyewall convection. This difference suggests that the outer rainband and developing outer eyewall convection have different circulation regimes.

Barnes and Powell (1995) also noted this distinction in circulations in their examination of a rainband in Hurricane Gilbert, which was actually part of a developing outer eyewall forming at an unusually large radius (Dodge et al. 1999). Their rainband circulation resembled that of the current outer eyewall observations rather than the outer rainband circulations from past studies. They also noted that their observed thermodynamic structure was similar to that of an eyewall,

having a vertically stratified contour pattern of θ_e. Like that seen in the current Gonzalo observations, the developing outer eyewall in Gilbert acts as a barrier to low-level inflow. In addition to this barrier effect, Barnes and Powell (1995) argued that the absence of downdrafts originating from midlevel inflow in this circulation pattern has a positive effect on the inner eyewall intensity—the lack of boundary layer low-θ_e approaching the eyewall allows for intensification. While this positive impact may occur initially, the current study argues that the barrier effect eventually has a more important contribution to determining the inner eyewall intensity evolution.

Zhou and Wang (2011) argued in favor of the outer eyewall barrier effect by showing that large inward radial advection of θ_e into the inner eyewall reduces the inflow of moist, warm air necessary to feed its convection. They noted that the barrier effect is most notable when the two eyewalls are close to each other. In outer primary 2, the distance between the eyewalls is close to 30 km, which is about the same distance as in Zhou and Wang (2011; cf. their Fig. 9). Although the full thermodynamic field was not available in Gonzalo, these similar separation distances indicate that negative radial advection of θ_e plausibly contributed to the demise of Gonzalo's inner eyewall on 15 October.

Bell et al. (2012) found in their analysis of Hurricane Rita that boundary layer inflow and low-level convergence of the outer eyewall increased while that of the inner eyewall decreased, which they argued supported the barrier effect. They also found that an asymmetric deep inner eyewall updraft remained robust and deeper than that of the outer eyewall's, such that the existing forced descent from the outer eyewall was likely not strong enough to counteract the inner eyewall updraft. The current observations here do not indicate a deep updraft in the inner eyewall at the outer primary times. Moreover, the downshear quadrants in Fig. 14 do show evidence of descent from the outer eyewall that is overriding the updraft of a decaying inner eyewall. In this study, we are not arguing against the suppression mechanism, as it could very well be working together with the barrier effect to suppress the inner eyewall toward the end of an eyewall replacement cycle.

9. Conclusions

This study examined the kinematics of two eyewall replacement cycles observed by airborne radar in Hurricane Gonzalo. During two consecutive days, the NOAA P3 TA radar and the NASA HIWRAP radar captured Gonzalo's concentric eyewalls at four stages of the eyewall replacement cycle. These snapshots of data
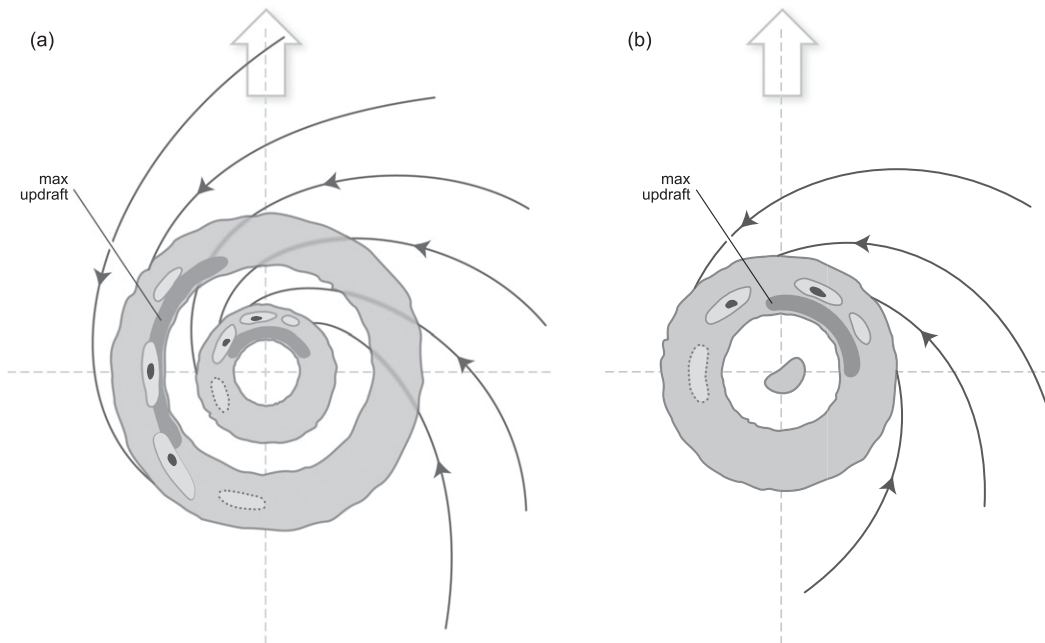
FIG. 16. (a),(b) Plan view schematic of eyewall structures during an eyewall replacement cycle. The concentric eyewall pattern in (a) occurs when the storm's maximum winds are located at the inner eyewall, and the eyewall pattern in (b) occurs later when the storm's maximum winds are located at the larger, outer eyewall. The environmental wind shear vector, indicated by block arrows, points upward and divides the four quadrants of the storm along the gray dashed lines. Shaded rings represent reflectivity pattern of closed eyewalls. Embedded within each ring are convective cells of higher reflectivity asymmetrically distributed. Selected streamlines of boundary layer winds show air spiraling inward toward the eyewalls. The maximum updraft region in each eyewall is shaded dark gray.

were analyzed in relation to the environmental wind shear and in a relative time framework centered upon the time of minimum central pressure for each eyewall replacement cycle.

Figure 16 presents a conceptual model that summarizes the results of this study. At the inner primary times (when the maximum winds were located at the inner eyewall; Fig. 16a), low-level flow spiraled radially inward toward the developing concentric eyewalls in an asymmetry that differed between the two eyewalls. The kinematic asymmetry at the inner eyewall was consistent with the asymmetry expected from vortex interaction with the environmental wind shear (Braun et al. 2006; Reasor et al. 2013; Zhang et al. 2013). The inflow layer was consistently strong and deep (reaching ~4-km altitude) in the DR quadrant. Here, inward-spiraling air reached the outer eyewall first and passed through to the inner eyewall. This low-level flow into the inner eyewall turned upward to produce the strongest inner eyewall updrafts in the DR and DL quadrants. Traveling downwind, the inflow layer became shallower and eventually subsided at the inner eyewall, but continued at the outer eyewall in the left-of-shear quadrants. Here, the low-level inflow turned upward to produce the strongest outer eyewall updrafts. The different radial

and vertical velocity asymmetries at each eyewall directly impact the low-level tangential wind acceleration pattern through contributions from the advective tendency terms [Eq. (1)]. The downwind shift in maximum updrafts is consistent with the downwind shift of outer eyewall convective cells examined by Hence and Houze (2012a), which is also depicted in the conceptual model.

We argue that the downwind extension of radial flow into the outer eyewall signals a barrier effect that contributes to the decay of the inner eyewall toward the end of eyewall replacement. Some of the inward-spiraling low-level air experiences convergence and turns upward at the outer eyewall before reaching the inner eyewall. If the outer eyewall were not extracting low-level inflow at the expense of the inner eyewall, we would expect a radial flow asymmetry where outer eyewall inflow stopped upwind of the inner eyewall inflow, given the spiral nature of the low-level flow. Instead, Gonzalo exhibited the opposite pattern, which supports the outer eyewall barrier and inner eyewall weakening argument asserted by past studies (Samsury and Zipser 1995; Zhou and Wang 2011; Bell et al. 2012).

In the outer primary times (when the maximum winds were located at the outer eyewall; Fig. 16b), the outer

eyewall contracts and becomes the primary eyewall of the storm, as the older inner eyewall decays. Compared to the outer eyewall from the inner primary times, strong low-level inflow and maximum updrafts shift upwind, and the outer eyewall exhibits a circulation pattern more like the earlier inner eyewall. This asymmetry is now consistent with that expected from vortex interaction with the environmental wind shear.

The reason for the azimuthal shift of maximum low-level inflow and updrafts does not come readily in consideration of past studies. We speculate that the early outer eyewall asymmetry results from interaction with a spiral rainband complex that is merging with the developing outer eyewall. The same wind shear dynamics involved in the inner eyewall asymmetry may not initially be influencing the outer eyewall asymmetry. But as the outer eyewall becomes the primary eyewall over time, these dynamics would become more influential, leading to the upwind shift in the kinematic and convection asymmetry.

This study is certainly limited as it involves only a single storm under specific circumstances. As a result, some of the current results may be specific to Hurricane Gonzalo. Other storms may have variations in their concentric eyewall evolution due to many different factors, such as shear direction, shear magnitude, storm intensity, storm track, and convective environmental conditions. Future studies must assess the representativeness of the current results by examining more storms under varying circumstances. Modeling studies are also needed to further examine the dynamical reasons for the observed asymmetries and kinematic evolution during an eyewall replacement cycle. This examination could include a wavenumber analysis that determines how each wavenumber asymmetry is evolving. Modeling studies will include analyses of pressure and friction, which are neglected in this study.

REFERENCES

Abarca, S. F., and M. T. Montgomery, 2013: Essential dynamics of secondary eyewall formation. *J. Atmos. Sci.*, **70**, 3216–3230, doi:10.1175/JAS-D-12-0318.1.

——, and ——, 2014: Departures from axisymmetric balance dynamics during secondary eyewall formation. *J. Atmos. Sci.*, **71**, 3723–3738, doi:10.1175/JAS-D-14-0018.1.

——, and ——, 2015: Are eyewall replacement cycles governed largely by axisymmetric balance dynamics? *J. Atmos. Sci.*, **72**, 82–87, doi:10.1175/JAS-D-14-0151.1.

Aberson, S. D., M. L. Black, R. A. Black, J. J. Cione, C. W. Landsea, F. D. Marks, and R. W. Burpee, 2006: Thirty years of tropical cyclone research with the NOAA P-3 aircraft. *Bull. Amer. Meteor. Soc.*, **87**, 1039–1055, doi:10.1175/BAMS-87-8-1039.

Barnes, G. M., and M. D. Powell, 1995: Evolution of the inflow boundary layer of Hurricane Gilbert (1988). *Mon. Wea. Rev.*, **123**, 2348–2368, doi:10.1175/1520-0493(1995)123<2348: EOTIBL>2.0.CO;2.

——, E. J. Zipser, D. Jorgensen, and F. Marks Jr., 1983: Mesoscale and convective structure of a hurricane rainband. *J. Atmos. Sci.*, **40**, 2125–2137, doi:10.1175/1520-0469(1983)040<2125: MACSOA>2.0.CO;2.

Bell, M. M., M. T. Montgomery, and W.-C. Lee, 2012: An axisymmetric view of concentric eyewall evolution in Hurricane Rita (2005). *J. Atmos. Sci.*, **69**, 2414–2432, doi:10.1175/JAS-D-11-0167.1.

Bender, M. A., 1997: The effect of relative flow on the asymmetric structure in the interior of hurricanes. *J. Atmos. Sci.*, **54**, 703–724, doi:10.1175/1520-0469(1997)054<0703:TEORFO>2.0.CO;2.

Black, M. L., and H. E. Willoughby, 1992: The concentric eyewall cycle of Hurricane Gilbert. *Mon. Wea. Rev.*, **120**, 947–957, doi:10.1175/1520-0493(1992)120<0947:TCECOH>2.0.CO;2.

——, R. W. Burpee, and F. D. Marks Jr., 1996: Vertical motion characteristics of tropical cyclones determined with airborne Doppler radial velocities. *J. Atmos. Sci.*, **53**, 1887–1909, doi:10.1175/1520-0469(1996)053<1887:VMCOTC>2.0.CO;2.

——, J. F. Gamache, F. D. Marks Jr., C. E. Samsury, and H. E. Willoughby, 2002: Eastern Pacific Hurricanes Jimena of 1991 and Olivia of 1994: The effect of vertical shear on structure and intensity. *Mon. Wea. Rev.*, **130**, 2291–2312, doi:10.1175/1520-0493(2002)130<2291:EPHJOA>2.0.CO;2.

Braun, S. A., 2002: A cloud-resolving simulation of Hurricane Bob (1991): Storm structure and eyewall buoyancy. *Mon. Wea. Rev.*, **130**, 1573–1592, doi:10.1175/1520-0493(2002)130<1573: ACRSOH>2.0.CO;2.

——, M. T. Montgomery, and Z. Pu, 2006: High-resolution simulation of Hurricane Bonnie (1998). Part I: The organization of eyewall vertical motion. *J. Atmos. Sci.*, **63**, 19–42, doi:10.1175/JAS3598.1.

——, and Coauthors, 2013: NASA's Genesis and Rapid Intensification Processes (GRIP) Field Experiment. *Bull. Amer. Meteor. Soc.*, **94**, 345–363, doi:10.1175/BAMS-D-11-00232.1.

——, P. A. Newman, and G. M. Heymsfield, 2016: NASA's Hurricane and Severe Storm Sentinel (HS3) investigation. *Bull. Amer. Meteor. Soc.*, **97**, 2085–2102, doi:10.1175/BAMS-D-15-00186.1.

Chen, H., D.-L. Zhang, J. Carton, and R. Atlas, 2011: On the rapid intensification of Hurricane Wilma (2005). Part I: Model prediction and structural changes. *Wea. Forecasting*, **26**, 885–901, doi:10.1175/WAF-D-11-00001.1.

Chen, S. S., J. A. Knaff, and F. D. Marks Jr., 2006: Effects of vertical wind shear and storm motion on tropical cyclone rainfall asymmetries deduced from TRMM. *Mon. Wea. Rev.*, **134**, 3190–3208, doi:10.1175/MWR3245.1.

Corbosiero, K. L., and J. Molinari, 2002: The effects of vertical wind shear on the distribution of convection in tropical cyclones. *Mon. Wea. Rev.*, **130**, 2110–2123, doi:10.1175/1520-0493(2002)130<2110:TEOVWS>2.0.CO;2.

——, and ——, 2003: The relationship between storm motion, vertical wind shear, and convective asymmetries in tropical cyclones. *J. Atmos. Sci.*, **60**, 366–460, doi:10.1175/1520-0469(2003)060<0366:TRBSMV>2.0.CO;2.

DeHart, J. C., R. A. Houze Jr., and R. F. Rogers, 2014: Quadrant distribution of tropical cyclone inner-core kinematics in relation to environmental shear. *J. Atmos. Sci.*, **71**, 2713–2732, doi:10.1175/JAS-D-13-0298.1.

DeMaria, M., M. Mainelli, L. K. Shay, J. A. Knaff, and J. Kaplan, 2005: Further improvements to the Statistical Hurricane Intensity Prediction Scheme (SHIPS). *Wea. Forecasting*, **20**, 531–543, doi:10.1175/WAF862.1.

Didlake, A. C., Jr., and R. A. Houze Jr., 2009: Convective-scale downdrafts in the principal rainband of Hurricane Katrina (2005). *Mon. Wea. Rev.*, **137**, 3269–3293, doi:10.1175/2009MWR2827.1.

——, and ——, 2011: Kinematics of the secondary eyewall observed in Hurricane Rita (2005). *J. Atmos. Sci.*, **68**, 1620–1636, doi:10.1175/2011JAS3715.1.

——, and ——, 2013a: Convective-scale variations in the inner-core rainbands of tropical cyclones. *J. Atmos. Sci.*, **70**, 504–523, doi:10.1175/JAS-D-12-0134.1.

——, and ——, 2013b: Dynamics of the stratiform sector of a tropical cyclone rainband. *J. Atmos. Sci.*, **70**, 1891–1911, doi:10.1175/JAS-D-12-0245.1.

——, G. M. Heymsfield, L. Tian, and S. R. Guimond, 2015: The coplane analysis technique for three-dimensional wind retrieval using the HIWRAP airborne Doppler radar. *J. Appl. Meteor.*, **54**, 605–623, doi:10.1175/JAMC-D-14-0203.1.

Dodge, P., R. W. Burpee, and F. D. Marks Jr., 1999: The kinematic structure of a hurricane with sea level pressure less than 900 mb. *Mon. Wea. Rev.*, **127**, 987–1004, doi:10.1175/1520-0493(1999)127<0987:TKSOAH>2.0.CO;2.

Fierro, A. O., R. F. Rogers, and F. D. Marks Jr., 2009: The impact of horizontal grid spacing on the microphysical and kinematic structures of strong tropical cyclones simulated with the WRF-ARW model. *Mon. Wea. Rev.*, **137**, 3717–3743, doi:10.1175/2009MWR2946.1.

Frank, W. M., and E. A. Ritchie, 1999: Effects of environmental flow upon tropical cyclone structure. *Mon. Wea. Rev.*, **127**, 2044–2061, doi:10.1175/1520-0493(1999)127<2044:EOEFUT>2.0.CO;2.

——, and ——, 2001: Effects of vertical wind shear on the intensity and structure of numerically simulated hurricanes. *Mon. Wea. Rev.*, **129**, 2249–2269, doi:10.1175/1520-0493(2001)129<2249:EOVWSO>2.0.CO;2.

Gamache, J. F., 1997: Evaluation of a fully three-dimensional variational Doppler analysis technique. Preprints, *28th Conf. on Radar Meteorology,* Austin, TX, Amer. Meteor. Soc., 422–423.

Gao, J., M. Xue, A. Shapiro, and K. K. Droegemeier, 1999: A variational method for the analysis of three-dimensional wind fields from two Doppler radars. *Mon. Wea. Rev.*, **127**, 2128–2142, doi:10.1175/1520-0493(1999)127<2128:AVMFTA>2.0.CO;2.

Gu, J.-F., Z.-M. Tan, and X. Qiu, 2016: Quadrant-dependent evolution of low-level tangential wind of a tropical cyclone in the shear flow. *J. Atmos. Sci.*, **73**, 1159–1177, doi:10.1175/JAS-D-15-0165.1.

Guimond, S. R., L. Tian, G. M. Heymsfield, and S. J. Frasier, 2014: Wind retrieval algorithms for the IWRAP and HIWRAP

airborne Doppler radars with application to hurricanes. *J. Atmos. Oceanic Technol.*, **31**, 1189–1215, doi:10.1175/JTECH-D-13-00140.1.

——, G. M. Heymsfield, P. D. Reasor, and A. C. Didlake Jr., 2016: The rapid intensification of Hurricane Karl (2010): New remote sensing observations of convective bursts from the Global Hawk platform. *J. Atmos. Sci.*, **73**, 3617–3639, doi:10.1175/JAS-D-16-0026.1.

Hence, D. A., and R. A. Houze Jr., 2008: Kinematic structure of convective-scale elements in the rainbands of Hurricanes Katrina and Rita (2005). *J. Geophys. Res.*, **113**, D15108, doi:10.1029/2007JD009429.

——, and ——, 2011: Vertical structure of hurricane eyewalls as seen by the TRMM Precipitation Radar. *J. Atmos. Sci.*, **68**, 1637–1652, doi:10.1175/2011JAS3578.1.

——, and ——, 2012a: Vertical structure of tropical cyclones with concentric eyewalls as seen by the TRMM Precipitation Radar. *J. Atmos. Sci.*, **69**, 1021–1036, doi:10.1175/JAS-D-11-0119.1.

——, and ——, 2012b: Vertical structure of tropical cyclone rainbands as seen by the TRMM Precipitation Radar. *J. Atmos. Sci.*, **69**, 2644–2661, doi:10.1175/JAS-D-11-0323.1.

Houze, R. A., Jr., and Coauthors, 2006: The Hurricane Rainband and Intensity Change Experiment: Observations and modeling of Hurricanes Katrina, Ophelia, and Rita. *Bull. Amer. Meteor. Soc.*, **87**, 1503–1521, doi:10.1175/BAMS-87-11-1503.

——, S. S. Chen, B. F. Smull, W.-C. Lee, and M. M. Bell, 2007: Hurricane intensity and eyewall replacement. *Science*, **315**, 1235–1239, doi:10.1126/science.1135650.

Huang, Y.-H., M. T. Montgomery, and C.-C. Wu, 2012: Concentric eyewall formation in Typhoon Sinlaku (2008). Part II: Axisymmetric dynamical processes. *J. Atmos. Sci.*, **69**, 662–674, doi:10.1175/JAS-D-11-0114.1.

Jones, S. C., 1995: The evolution of vortices in vertical shear. I: Initially barotropic vortices. *Quart. J. Roy. Meteor. Soc.*, **121**, 821–851, doi:10.1002/qj.49712152406.

Jorgensen, D. P., and J. D. DuGranrut, 1991: A dual-beam technique for deriving wind fields from airborne Doppler radar. Preprints, *25th Int. Conf. on Radar Meteorology,* Paris, France, Amer. Meteor. Soc., 458–461.

Judt, F., and S. S. Chen, 2010: Convectively generated potential vorticity in rainbands and formation of the secondary eyewall in Hurricane Rita of 2005. *J. Atmos. Sci.*, **67**, 3581–3599, doi:10.1175/2010JAS3471.1.

Kepert, J. D., 2013: How does the boundary layer contribute to eyewall replacement cycles in axisymmetric tropical cyclones? *J. Atmos. Sci.*, **70**, 2808–2830, doi:10.1175/JAS-D-13-046.1.

Kossin, J. P., and W. H. Schubert, 2001: Mesovortices, polygonal flow patterns, and rapid pressure falls in hurricane-like vortices. *J. Atmos. Sci.*, **58**, 2196–2209, doi:10.1175/1520-0469(2001)058<2196:MPFPAR>2.0.CO;2.

Li, L., and Coauthors, 2016: The NASA high-altitude imaging wind and rain airborne profiler. *IEEE Trans. Geosci. Remote Sens.*, **54**, 298–310, doi:10.1109/TGRS.2015.2456501.

Lord, S. J., H. E. Willoughby, and J. M. Piotrowicz, 1984: Role of a parameterized ice-phase microphysics in an axisymmetric, non-hydrostatic tropical cyclone model. *J. Atmos. Sci.*, **41**, 2836–2848, doi:10.1175/1520-0469(1984)041<2836:ROAPIP>2.0.CO;2.

Montgomery, M. T., and R. J. Kallenbach, 1997: A theory for vortex Rossby-waves and its application to spiral bands and intensity changes in hurricanes. *Quart. J. Roy. Meteor. Soc.*, **123**, 435–465, doi:10.1002/qj.49712353810.

Powell, M. D., 1990a: Boundary layer structure and dynamics in outer hurricane rainbands. Part I: Mesoscale rainfall and

kinematic structure. *Mon. Wea. Rev.*, **118**, 891–917, doi:10.1175/1520-0493(1990)118<0891:BLSADI>2.0.CO;2.

——, 1990b: Boundary layer structure and dynamics in outer hurricane rainbands. Part II: Downdraft modification and mixed layer recovery. *Mon. Wea. Rev.*, **118**, 918–938, doi:10.1175/1520-0493(1990)118<0918:BLSADI>2.0.CO;2.

Qiu, X., and Z.-M. Tan, 2013: The roles of asymmetric inflow forcing induced by outer rainbands in tropical cyclone secondary eyewall formation. *J. Atmos. Sci.*, **70**, 953–974, doi:10.1175/JAS-D-12-084.1.

Reasor, P. D., and M. D. Eastin, 2012: Rapidly intensifying Hurricane Guillermo (1997). Part II: Resilience in shear. *Mon. Wea. Rev.*, **140**, 425–444, doi:10.1175/MWR-D-11-00080.1.

——, ——, and J. F. Gamache, 2009: Rapidly intensifying Hurricane Guillermo (1997). Part I: Low-wavenumber structure and evolution. *Mon. Wea. Rev.*, **137**, 603–631, doi:10.1175/2008MWR2487.1.

——, R. F. Rogers, and S. Lorsolo, 2013: Environmental flow impacts on tropical cyclone structure diagnosed from airborne Doppler radar composites. *Mon. Wea. Rev.*, **141**, 2949–2969, doi:10.1175/MWR-D-12-00334.1.

Riemer, M., 2016: Meso-β-scale environment for the stationary band complex of vertically sheared tropical cyclones. *Quart. J. Roy. Meteor. Soc.*, **142**, 2442–2451, doi:10.1002/qj.2837.

——, M. T. Montgomery, and M. E. Nicholls, 2010: A new paradigm for intensity modification of tropical cyclones: Thermodynamic impact of vertical wind shear on the inflow layer. *Atmos. Chem. Phys.*, **10**, 3163–3188, doi:10.5194/acp-10-3163-2010.

Rogers, R. F., S. S. Chen, J. Tenerelli, and H. E. Willoughby, 2003: A numerical study of the impact of vertical shear on the distribution of rainfall in Hurricane Bonnie (1998). *Mon. Wea. Rev.*, **131**, 1577–1599, doi:10.1175//2546.1.

——, S. Lorsolo, P. Reasor, J. Gamache, and F. Marks, 2012: Multiscale analysis of tropical cyclone kinematic structure from airborne Doppler radar composites. *Mon. Wea. Rev.*, **140**, 77–99, doi:10.1175/MWR-D-10-05075.1.

——, P. D. Reasor, and J. A. Zhang, 2015: Multiscale structure and evolution of Hurricane Earl (2010) during rapid intensification. *Mon. Wea. Rev.*, **143**, 536–562, doi:10.1175/MWR-D-14-00175.1.

Rozoff, C. M., W. H. Schubert, and J. P. Kossin, 2008: Some dynamical aspects of tropical cyclone concentric eyewalls. *Quart. J. Roy. Meteor. Soc.*, **134**, 583–593, doi:10.1002/qj.237.

——, D. S. Nolan, J. P. Kossin, F. Zhang, and J. Fang, 2012: The roles of an expanding wind field and inertial stability in tropical cyclone secondary eyewall formation. *J. Atmos. Sci.*, **69**, 2621–2643, doi:10.1175/JAS-D-11-0326.1.

Samsury, C. E., and E. J. Zipser, 1995: Secondary wind maxima in hurricanes: Airflow and relationship to rainband. *Mon. Wea. Rev.*, **123**, 3502–3517, doi:10.1175/1520-0493(1995)123<3502:SWMIHA>2.0.CO;2.

Shapiro, L. J., and H. E. Willoughby, 1982: The response of balanced hurricanes to local sources of heat and momentum. *J. Atmos. Sci.*, **39**, 378–394, doi:10.1175/1520-0469(1982)039<0378:TROBHT>2.0.CO;2.

Sitkowski, M., J. P. Kossin, and C. M. Rozoff, 2011: Intensity and structure changes during hurricane eyewall replacement cycles. *Mon. Wea. Rev.*, **139**, 3829–3847, doi:10.1175/MWR-D-11-00034.1.

——, ——, ——, and J. Knaff, 2012: Hurricane eyewall replacement cycle thermodynamics and the relict inner eyewall circulation. *Mon. Wea. Rev.*, **140**, 4035–4045, doi:10.1175/MWR-D-11-00349.1.

Smith, R. K., M. T. Montgomery, and S. V. Nguyen, 2009: Tropical cyclone spin-up revisited. *Quart. J. Roy. Meteor. Soc.*, **135**, 1321–1335, doi:10.1002/qj.428.

Stern, D. P., and D. S. Nolan, 2009: Reexamining the vertical structure of tangential winds in tropical cyclones: Observations and theory. *J. Atmos. Sci.*, **66**, 3579–3600, doi:10.1175/2009JAS2916.1.

Sun, Y. Q., Y. Jiang, B. Tan, and F. Zhang, 2013: The governing dynamics of the secondary eyewall formation of Typhoon Sinlaku (2008). *J. Atmos. Sci.*, **70**, 3818–3837, doi:10.1175/JAS-D-13-044.1.

Tian, L., G. M. Heymsfield, A. C. Didlake Jr., S. Guimond, and L. Li, 2015: Velocity–azimuth display analysis of Doppler velocity for HIWRAP. *J. Appl. Meteor. Climatol.*, **54**, 1792–1808, doi:10.1175/JAMC-D-14-0054.1.

Vigh, J. L., and Coauthors, 2016: FLIGHT+: The extended flight level dataset for tropical cyclones (version 1.1). Tropical Cyclone Data Project, National Center for Atmospheric Research, Research Applications Laboratory, Boulder, CO, doi:10.5065/D6WS8R93, accessed 21 July 2016.

Willoughby, H. E., 1988: The dynamics of the tropical hurricane core. *Aust. Meteor. Mag.*, **36**, 183–191.

——, and M. B. Chelmow, 1982: Objective determination of hurricane tracks from aircraft observations. *Mon. Wea. Rev.*, **110**, 1298–1305, doi:10.1175/1520-0493(1982)110<1298:ODOHTF>2.0.CO;2.

——, J. A. Clos, and M. G. Shoreibah, 1982: Concentric eye walls, secondary wind maxima, and the evolution of the hurricane vortex. *J. Atmos. Sci.*, **39**, 395–411, doi:10.1175/1520-0469(1982)039<0395:CEWSWM>2.0.CO;2.

——, F. D. Marks Jr., and R. J. Feinberg, 1984: Stationary and moving convective bands in hurricanes. *J. Atmos. Sci.*, **41**, 3189–3211, doi:10.1175/1520-0469(1984)041<3189:SAMCBI>2.0.CO;2.

Wu, L., S. A. Braun, J. Halverson, and G. Heymsfield, 2006: A numerical study of Hurricane Erin (2001). Part I: Model verification and storm evolutionary. *J. Atmos. Sci.*, **63**, 65–86, doi:10.1175/JAS3597.1.

Yang, Y.-T., H.-C. Kuo, E. A. Hendricks, and M. S. Peng, 2013: Structural and intensity changes of concentric eyewall typhoons in the western North Pacific basin. *Mon. Wea. Rev.*, **141**, 2632–2648, doi:10.1175/MWR-D-12-00251.1.

Zhang, J. A., R. F. Rogers, P. D. Reasor, E. W. Uhlhorn, and F. D. Marks, 2013: Asymmetric hurricane boundary layer structure from dropsonde composites in relation to the environmental vertical wind shear. *Mon. Wea. Rev.*, **141**, 3968–3984, doi:10.1175/MWR-D-12-00335.1.

Zhou, X., and B. Wang, 2011: Mechanism of concentric eyewall replacement cycles and associated intensity change. *J. Atmos. Sci.*, **68**, 972–988, doi:10.1175/2011JAS3575.1.

Zhu, T., D.-L. Zhang, and F. H. Weng, 2004: Numerical simulation of Hurricane Bonnie (1998). Part I: Eyewall evolution and intensity changes. *Mon. Wea. Rev.*, **132**, 225–241, doi:10.1175/1520-0493(2004)132<0225:NSOHBP>2.0.CO;2.

Zhu, Z., and P. Zhu, 2014: The role of outer rainband convection in governing the eyewall replacement cycle in numerical simulations of tropical cyclones. *J. Geophys. Res. Atmos.*, **119**, 8049–8072, doi:10.1002/2014JD021899.

Zipser, E. J., 2003: Some views on "hot towers" after 50 years of tropical field programs and two years of TRMM data. *Cloud Systems, Hurricanes, and the Tropical Rainfall Measuring Mission (TRMM)—A Tribute to Dr. Joanne Simpson, Meteor. Monogr.*, No. 51, Amer. Meteor. Soc., 49–58, doi:10.1175/0065-9401(2003)029<0049:CSVOHT>2.0.CO;2.